

A KECK HIRES INVESTIGATION OF THE METAL ABUNDANCES AND KINEMATICS OF THREE DAMPED $\text{Ly}\alpha$ SYSTEMS TOWARD Q2206–199

JASON X. PROCHASKA & ARTHUR M. WOLFE¹

Department of Physics, and Center for Astrophysics and Space Sciences;
University of California, San Diego;
C-0111; La Jolla; CA 92093-0111

ABSTRACT

We present high resolution, high SNR spectra of the QSO Q2206-199 obtained with HIRES on the 10m W.M. Keck Telescope. Our analysis focuses on the two previously identified damped $\text{Ly}\alpha$ systems found at $z = 1.920$ and $z = 2.076$. For the $z = 1.920$ system, we measure accurate abundances (relative to solar) for Fe, Cr Si, Ni, Ti, and Zn: $[\text{Fe}/\text{H}] = -0.705 \pm 0.097$, $[\text{Cr}/\text{H}] = -0.580 \pm 0.100$, $[\text{Si}/\text{H}] = -0.402 \pm 0.098$, $[\text{Ni}/\text{H}] = -1.012 \pm 0.095$, $[\text{Ti}/\text{H}] = -0.776 \pm 0.081$, and $[\text{Zn}/\text{H}] = -0.379 \pm 0.097$. This system exhibits the highest metallicity we have measured for a damped $\text{Ly}\alpha$ system. By contrast the $z = 2.076$ system is the most metal poor ($[\text{Zn}/\text{H}] < -1.745$) we have analyzed, showing absorption features for only the strongest transitions. We determine accurate abundances for Fe, Si and Al: $[\text{Fe}/\text{H}] = -2.621 \pm 0.071$, $[\text{Si}/\text{H}] = -2.225 \pm 0.075$, and $[\text{Al}/\text{H}] = -2.727 \pm 0.070$.

Analyses of the abundance variations of Fe, Ni, Cr, and Si relative to Zn and the abundance trends versus condensation temperature do not offer positive evidence for the presence of dust in the damped system at $z = 1.920$. In addition, the relative abundance ratio $[\text{Ti}/\text{Fe}] \approx 0$ further suggests the absence of ISM-like dust. Unfortunately, the lack of measurable Zn absorption in the $z = 2.076$ system does not allow a similar investigation for the presence of dust.

In addition to the significant difference in metallicity, the two damped systems have vastly different kinematic characteristics. The $z = 1.920$ system spans $\approx 150 \text{ km s}^{-1}$ in velocity space (measured from the low-ion transitions) while the $z = 2.076$ system spans a mere 30 km s^{-1} . Furthermore, the $z = 1.920$ profiles are significantly asymmetric while the $z = 2.076$ profiles are

¹Visiting Astronomer, W.M. Keck Telescope. The Keck Observatory is a joint facility of the University of California and the California Institute of Technology.

highly symmetric. Even with these differences, we contend the two systems are consistent with one physical description, that of a thick, rotating disk.

In addition to the two previously identified damped Ly α systems, we investigate a very strong Mg II system at $z = 0.752$ which is very likely yet a third damped Ly α system along the line of sight. The very weak Mn II 2606, 2594, 2576 and Ti II 3073, 3342, and 3384 transitions have been positively measured and suggest a very conservative lower limit H I abundance of $\log N(\text{HI}) > 19.0$ assuming metallicity relative to solar equal to 0 and no depletion. Together with the damped system at $z = 1.920$, this marks the first confident ($> 5\sigma$) detection of Ti in QSO absorption line systems. We analyze the abundance ratios [Mn/Fe] and [Ti/Fe] and their values are inconsistent with dust depletion, yet consistent with the abundance pattern detected for halo stars in the Galaxy (Lu et al. 1996a).

Finally, we identify a C IV system at $z = 2.014$ that shows a very narrow feature in Si IV and C IV absorption. The corresponding b values (5.5 km s^{-1} and 8.9 km s^{-1} for Si IV and C IV respectively) for this component suggest a temperature of $4.7 \times 10^4 \text{ K}$. Because collisional ionization can explain the observed abundances only for $T > 8 \times 10^4 \text{ K}$, we contend these ions must have formed through a different physical process (e.g. photoionization).

Subject headings: galaxies: evolution—galaxies: formation—absorption lines—quasars: individual (Q2206–199)—galaxies:abundances

1. INTRODUCTION

This paper is the third in a series devoted to studying the metal content of high-redshift galaxies and their progenitors with the 10m W.M. Keck Telescope. Our primary objectives are

- (1) to record the emergence of metals in galaxies,
- (2) to trace the mean cosmic metallicity from $z \approx 4.5$ to the present,
- (3) to determine the kinematic state of galaxies from $z \approx 4.5$ to the present.

We are implementing this study using HIRES, the echelle spectrograph on the Keck 10m Telescope (Vogt 1992), to obtain high-resolution spectra of QSOs with foreground damped Ly α systems. The damped Ly α systems are a population of neutral gas layers exhibiting properties indicating they are either galaxy progenitors, or well formed galaxies detected

during an early evolutionary phase. Recent studies indicate the comoving density of neutral gas in damped systems at $z \approx 3.3$ is comparable to the density of visible stars in current galaxies. At lower redshifts, the comoving density of neutral gas decreases with time in a manner consistent with gas consumption by star formation (Wolfe et al. 1995), and at higher redshifts there is tentative evidence for an increase in comoving density with time possibly indicating accretion of gas (Storrie-Lombardi et al. 1995). Therefore, studies of the metal content of the damped Ly α systems enable one to trace the chemical evolution of representative galaxies from a presumably metal-poor gaseous progenitor phase to metal-rich epochs when most of the baryons are in stars. As a result the age-metallicity relation, kinematic conditions, etc., deduced from the damped Ly α systems should tell us more about the history of galaxies at large redshifts than analogous relations deduced from old stars found in the solar neighborhood (Evardsson et al. 1993).

In previous papers we have examined two damped Ly α systems at $z = 2.309$ toward PHL 957 (Wolfe et al. 1994) and at $z = 2.462$ toward Q0201+365 (Prochaska and Wolfe 1996a). We derived metallicities² from the Zn abundances of $[Z/H] = -1.55 \pm 0.11$ and $[Z/H] > -0.562$ respectively. Investigating the kinematics of the two systems from their low-ion velocity profiles, we noted a systematic edge-leading asymmetry where the majority of gas is found in at one edge with decreasing absorption toward the other edge. We contend that this edge-leading asymmetry is consistent with a thick rotating disk with rotation speeds $v \approx 200 \text{ km s}^{-1}$ which resembles the kinematics of our own Galaxy. Finally, we estimated the dust content of the damped system toward Q0201+365 by studying the variations in the abundances of Fe, Si, Ni, and Cr relative to Zn (Zn has very low levels of adsorption onto dust grains). Our analysis suggests this system is relatively free of dust grains.

This paper presents HIRES spectra for Q2206–199, a $V = 17.3$ QSO with emission redshift $z_{em} = 2.56$. We focus this study on two damped Ly α systems at $z = 1.920$ and $z = 2.076$ examined previously by several authors (Bergeron and Petitjean 1991, Rauch et al. 1990, Robertson et al. 1983, Rauch et al. 1993). Pettini et al. (1994) have fitted a Voigt damping profile to the Ly α absorption troughs at $z = 1.920$ and $z = 2.076$ and found $N(\text{HI}) = 4.5 \pm 0.8 \times 10^{20} \text{ cm}^{-2}$ and $N(\text{HI}) = 2.7 \pm 0.4 \times 10^{20} \text{ cm}^{-2}$ respectively. Because the system at $z = 1.920$ is very metal rich, relatively good measurements of the abundances of Cr, Zn, and Si have been made with lower resolution data (Bergeron and Petitjean 1991, Pettini et al. 1994). That work has a limited wavelength coverage and a relatively low signal to noise ratio (SNR). Therefore an analysis of the abundances of Ni and Fe could not

²Note that the use of Zn as the indicator of metallicity is now in question. See §5.1.1 below.

be successfully performed. Rauch et al. (1990) have examined the $z = 2.076$ damped Ly α system with moderate resolution ($\approx 30 \text{ km s}^{-1}$) and SNR. Their observations were limited to the Ly α forest, however, and therefore suffered from contamination by Ly α clouds. They did, however, confirm the very low abundance of the $z = 2.076$ system first noted by Robertson et al. (1983). Finally, Pettini et al. (1994) have placed upper limits on the Zn and Cr abundances.

In the present study we obtain spectra at a resolution of $\approx 8 \text{ km s}^{-1}$ with a typical signal-to-noise ratio of 45:1 spanning $\approx 2500 \text{ \AA}$ from $\approx 4000 - 6500 \text{ \AA}$. The high quality of the spectra allows us to focus on weak unsaturated transitions of ions expected to dominate the ionization state of gas in neutral clouds. In addition, we are able to concentrate on transitions outside of the Ly α forest. In the following analysis of the $z = 1.920$ system, we establish accurate abundances relative to H for Ti, Fe, Ni, Si, Cr, and Zn and estimate the abundances of Cu and Ge. We also examine the abundance of Fe, Si, Ni and Cr relative to Zn in order to investigate the level of dust grain depletion. For the metal poor damped Ly α system at $z = 2.076$, we accurately measure abundances for Fe, Si, and Al and place a strict upper limit on the abundance of Zn and Ni. In addition to the detailed abundance measurements, we investigate the kinematic characteristics associated with the two damped Ly α systems. Finally, we analyze several significant Mg II and C IV systems identified toward Q2206-199.

The paper is organized as follows. §2 briefly reviews the acquisition and reduction of the HIRES data. We present the spectra in Figure 1 and an extensive absorption line list in Table 3. In §3, we present velocity profile plots and least-squares fits of the more extensive metal line systems. We utilize the results of the least-squares fits and the apparent optical depth method to determine ionic column densities of the most significant metal line systems in §4. §5 gives the abundances (measured relative to solar) of the 2 confirmed damped Ly α systems and a third possible damped Ly α system. We also look for variations of the relative abundances with respect to velocity in the $z = 1.920$ system. In §6, we investigate the kinematic characteristics of the 2 damped Ly α systems, comparing them with one another as well as with previous results for other damped Ly α systems. Finally, §7 gives a summary of the results.

2. DATA

In this section we present the HIRES spectra, detailing the techniques used for the acquisition and reduction of the data. Table 3 gives an absorption line list with measured equivalent widths and 1σ errors and identifies over 85% of the features redward of the Ly α

forest.

2.1. Acquisition

We observed Q2206-199 with the HIRES echelle spectrograph on the 10m W. M. Keck Telescope for 6.2 hours of total integration time over three nights of observation. A journal of the observation dates, exposure times, wavelength coverages and resolution of the data are presented in Table 1. We used the C5 decker plate with 1.1" slit, the kv380 filter to eliminate 2nd order blue wavelengths, and standard 2×1 binning on the 2048 x 2048 Tektronix CCD. As Table 1 indicates, we used two different CCD alignments covering two different wavelength regions for our observations. The setup provided a resolution (FWHM) ranging from 7.2 – 8.0 km s⁻¹ and wavelength coverage from 3940 – 6520 Å over 36 orders. There are gaps in the wavelength coverage between successive orders for orders redward of 5100 Å where the free spectral range of the echelle exceeds the format of the CCD. We also took ≈ 700 s exposures of the standard star BD+28411, 1s Th-Ar arc images, dark (bias) frames and flat fields for calibration.

2.2. Reduction

We reduced the data with the techniques discussed in Prochaska and Wolfe (1996a). In short, we utilized a software package kindly provided by T. Barlow (1996) to convert the 2-D CCD images to uncalibrated 1-D spectra. We then continuum fit the data with Legendre polynomials and wavelength calibrated to proper vacuum heliocentric wavelengths with the Th-Ar arc frames and the standard IRAF package *id*. We also derived a 1σ error array from the data assuming Poisson statistics while ignoring the errors associated with continuum fitting (i.e. $\sigma = \sqrt{N_{\text{obj}} + N_{\text{sky}}}$). Table 2 lists the average SNR for several orders of the spectra. There is a significant decrease in the SNR for wavelengths blueward of ≈ 4140 Å both because of the shorter total integration time and the insensitivity of HIRES at bluer wavelengths. Figure 1 presents the spectra (solid line) along with the 1σ error array (dotted line).

2.3. Absorption Lines

Table 3 lists the wavelengths, equivalent widths and 1σ errors for all absorption line features which exceed the 5σ limit in equivalent width as measured by techniques similar

to those of Lanzetta et al. (1991). The reported wavelengths represent rough estimates of the centroids of complex line profiles and should be taken only as guides for differentiating between features. We do not report equivalent widths for those features identified as sky absorption lines or complicated multiple transition blends.

Table 3 includes the transition names and approximate redshifts of those features we successfully identified. Identification proceeds in a largely *ad hoc* fashion, with the initial emphasis placed on finding C IV, Mg II and Si IV doublets. Having composed a list of redshifts for the metal-line systems, we attempt to match the remaining features with the strongest metal-line transitions. Finally, we compare the line profiles of the individual transitions of the redshift systems in velocity space for conclusive identification. Note that the vast majority of unidentified features blueward of 4350 Å are presumed to be Ly α lines.

By comparing the object frames with the identically reduced sky and standard star images, we identified night-sky absorption features in the spectra. These features are labeled appropriately in Table 3 along with all other identified spurious features.

3. ANALYSIS

This section presents the velocity profiles for the most complex metal line absorption systems toward Q2206-199. In all plots, a dot-dashed vertical line is drawn for reference, usually identifying the strongest feature present. For clarity, we have plotted features not related to the given system with dotted lines. Table 4 lists the adopted wavelengths and oscillator strengths taken from Morton (1991) with the exception of Si, Zn, Cr and Fe where we adopt oscillator strengths and wavelengths from Tripp et al. (1995) and Cardelli and Savage (1995).

For several of the systems, we superimpose the solutions of the least-squares fits from the VPFIT package kindly provided by R. Carswell. The VPFIT package is a least-squares program which minimizes the χ^2 matrix of a multiple component Gaussian fit to line profiles. The package allows one to tie the redshift and b values (where the Doppler velocity b and velocity dispersion are related by $b = \sqrt{2}\sigma$) of a given component from ion to ion while allowing the column densities to vary individually. The package calculates errors in the fitted parameters based on both the SNR of the data and the quality of the fit.

3.1. Damped Ly α Systems

3.1.1. $z = 1.920$

Figure 2 presents the velocity profiles and VPFIT solutions of the low-ion transitions associated with the damped Ly α system at $z=1.920$. The velocity centroids for the Gaussian components of the fit are denoted by the short vertical lines above the Fe II 1611 profile. In our solution, we tied the b values and redshifts of each component from ion to ion and allowed for individual variations only in the column densities. We found that a minimum of 9 individual components were required to optimally fit the low-ion transitions. Our solution yields a reduced $\chi^2_\nu = 1.057$ with a corresponding probability $P_{\chi^2} = 0.152$. The majority of the error in the fit lies in the Ni II profiles, most likely due to hidden saturation at $v \approx 65$ km s $^{-1}$ (see §4.1.1).

We have removed a feature in the Zn II profile at $v = 17$ km s $^{-1}$ (indicated by the dotted line) identified as a poorly subtracted sky line. In addition, we have accounted for absorption from Mg I 2026 by introducing a single Mg I component (at $v = 0$ km s $^{-1}$ in the Mg I 2026 frame) in the VPFIT solution. Table 5a lists the redshift, b value and column density along with 1σ error of every velocity component in the VPFIT solution. The quality of the fit reflects the high degree to which the low-ion profiles track one another.

The VPFIT solutions and velocity profiles for the high-ion and Al III transitions are given in Figure 3. In this case the vertical lines above the Al III 1854 and C IV 1548 indicate the velocity centroids of the Gaussian components for the Al III and C IV solutions respectively. The Al III profile does track the low-ion profiles (much more so than the high-ion profiles) but not closely enough to yield a successful simultaneous solution. In particular, absorption observed in the Al III profile at $v \approx 30$ and 140 km s $^{-1}$ is not evident in the low-ion profiles. The results of the fits for Al III (and C IV) are listed in Table 5b. The Al III solution yields a reduced $\chi^2_\nu = 1.00$ with a probability $P_{\chi^2} = 0.5$ as expected for a one ion solution.

Although the high and low-ion transitions span the same velocity interval, the profiles are significantly different. For instance, the C IV profile is much less resolved and shows less absorption at $v \approx 100$ km s $^{-1}$. We chose not to fit Si IV because of its very poor SNR and blends with several Ly α lines. Note that the features at $v \approx 200$ km s $^{-1}$ in the C IV 1550 profile are blends with Fe II 2586 from the $z = 0.752$ system and were included in the C IV fit. The solution yields a relatively high reduced $\chi^2_\nu = 1.64$ which is entirely due to the blending in the C IV 1550 profile. In contrast, the reduced χ^2_ν value for the C IV 1548 profile alone is less than 1.

Those velocity profiles not fit with the VPFIT package are presented in Figure 4. The three Ni II transitions are found in the Ly α forest and therefore suffer from blending and

poor SNR. The Ti II 1910 transitions are blended with one another and are very weak. The Si II 1526, Fe II 1608 and Al II 1670 profiles are all saturated and therefore cannot be fitted successfully.

3.1.2. $z=2.076$

Figure 5 shows the velocity profiles and VPFIT solutions (where applicable) of the metal line transitions associated with the damped Ly α system at $z = 2.076$. As discussed below, this system has a very low metallicity and therefore exhibits very few metal line transitions. In the VPFIT solution for the low ions Fe II 1608 and Al II 1670 (with velocity centroids denoted above the Fe II 1608 profile) we found a 1 component fit was optimal. Although two or more components are likely present in the feature, the resolution is insufficient to resolve them. Introducing a second component overdetermines the solution and leads to large errors. We chose not to fit the other low-ion profiles because they lie in the Ly α forest and therefore have low SNR and possible Ly α contamination. Table 6 presents the results of the low-ion solution.

In contrast to the low-ions, the high-ion solution for C IV required 4 components and the Si IV solution 2 components (denoted by the vertical lines above the C IV 1548 and Si IV 1402 profiles). The b values and redshifts differ significantly between the two solutions as well as with the low-ion solution. Thus there appears to be an inherent difference between the high and low-ions as well as between the individual high-ions. This may be a result of absorption from different regions within the system or the presence of a multi-phase medium. The fits were both successful, $\chi^2_\nu = 0.654$, $P_{\chi^2} = 0.977$ for Si IV and $\chi^2_\nu = 1.032$, $P_{\chi^2} = 0.401$ for C IV. The results are given in Table 6.

3.2. Mg II Systems

3.2.1. $z = 0.752$

Figure 6 shows the velocity plots of the very strong Mg II system at $z = 0.752$. The system is so metal rich that nearly all of the Fe II and Mg II transitions are saturated. Conversely, the Mn II and Ti II transitions are so weak they are dominated by noise. Therefore we chose not to perform a least-squares fit.

3.2.2. $z = 0.948$

The velocity plots and VPFIT solutions for the Mg II system at $z = 0.948$ are presented in Figure 7. The vertical lines above the Fe II 2382 and Mg II 2796 profiles indicate the velocity centroids of the Gaussian components. Fe II 2344 was excluded from the least-squares fit because of blending with Mn II 2606 from the $z = 0.752$ system, while Fe II 2374 and Fe II 2586 were omitted given their very low SNR. The fit was reasonably successful yielding $\chi^2_\nu = 1.354$ with 3 components for the Fe II transitions and 5 components for the Mg II transitions. The solutions are listed in Table 7. Note the lack of Mg I absorption at $v = 55 \text{ km s}^{-1}$, possibly indicating a difference in the ionization state of the two absorption features.

3.2.3. $z=1.017$

Figure 8 shows the velocity profiles and VPFIT solutions of the Mg II system at $z = 1.017$. The velocity centroids of the Gaussian components are given by the vertical lines above the Fe II 2374 profile. The weak feature at $v = 150 \text{ km s}^{-1}$ is certainly real and may be considered associated with the stronger absorption system. Given the high degree of line saturation, we were able to perform a successful fit only to the unsaturated Fe II 2374, 2586 and Mg I 2852 profiles. The results of this fit are presented in Table 8. The solution has a rather high reduced $\chi^2_\nu = 1.36$ value primarily resulting from the Mg I solution. Because the solution follows the Mg I profile very closely (in contrast to the $z = 0.948$ system), we suspect we may have underestimated the error in the data in this region.

3.3. Other Systems

3.3.1. $z = 2.014$

The velocity profiles and VPFIT solutions for the high ions of the C IV system at $z = 2.014$ are plotted in Figure 9. Si IV 1402 is blended with MgII 2803 from the $z = 0.508$ system and was not included in the fit. The small vertical lines above the Si IV 1393 and C IV 1548 transitions denote the velocity centroids of the Gaussian components in the line-profile solution where we have added 3 components to fit the C IV profiles. The VPFIT solution (see Table 9) yields an excellent reduced $\chi^2_\nu = 1.008$ with probability $P_{\chi^2} = 0.45$.

For this system we allowed for the possibility that the Doppler broadening (b values) of the features is not entirely due to bulk motions. Specifically we allowed for thermal

broadening of the b values, which will yield different b values for ions with different masses ($b \propto m^{-\frac{1}{2}}$) even though the b values for a given feature are tied together. The solution suggests two components at $v \approx 0$ km s⁻¹ with very different physical properties. One is very narrow with b values of 8.0 km s⁻¹ and 5.2 km s⁻¹ for C IV and Si IV respectively. Assuming these values to be thermal in origin, we find the temperature $T = 4.7 \times 10^4$ K. The other component is broad, with b values of 38.7 km s⁻¹ and 25.3 km s⁻¹ ($T = 1 \times 10^6$ K) for C IV and Si IV respectively.

The ionic concentrations for C⁺³ and Si⁺³ formed through collisional ionization peak at $T = 10^5$ K and 8×10^4 K respectively (Cox 1970, Shull and Van Steenberg 1982). If collisional ionization were to explain the narrow component at a temperature of $T \approx 5 \times 10^4$ K, we would expect to see significant concentrations of the singly ionized species (C⁺ and Si⁺). Unfortunately the C II 1334 transition is lost in the Ly α forest, but we can perform an accurate measurement of Si II 1526. Measuring the equivalent width over the velocity region spanning the Si IV feature, we find a 3σ upper limit to the Si⁺ column density $N(\text{Si}^+) < 12.43$, which is considerably lower than the column density of Si IV. Therefore we contend the narrow component at $v \approx 0$ km s⁻¹ does not result from collisional ionization. Furthermore, the simultaneous presence of low and high ions is a suggests the ions are produced by a photoionization flux. York et al. (1984) were the first to report a C IV system in which that ion could not have arisen from collisional process, yet their results were tentative because of limited resolution and signal to noise. Hence, the C IV system at $z = 2.014$ serves as the first unambiguous detection of a C IV system formed through a process other than collisional ionization.

3.3.2. $z = 2.281$ and $z = 2.445$

Figure 10a is a velocity profile plot of the Ly α and C IV transitions from the C IV system at $z = 2.281$. Figure 10b shows Si II as well as the Ly α and C IV transitions from the $z = 2.445$ C IV system. C IV 1550 at $z = 2.281$ is blended to the blue by Ni II 1751 from the $z = 1.920$ system and to the red by an unidentified transition. The vertical dash-dot lines indicate the velocity centroid of the C IV systems and the vertical dashed lines mark the approximate velocity centroids of the Ly α profiles. The striking feature of these systems is the obvious displacement (≈ 40 km s⁻¹ for $z = 2.281$ and ≈ 100 km s⁻¹ for $z = 2.445$) of C IV absorption from the center of the Ly α profile. In contrast, the Si II profiles from the $z = 2.445$ system are more nearly centered on the Ly α profile. This clearly suggests C IV profiles do not generally track HI or low-ion transitions.

4. IONIC COLUMN DENSITIES

This section presents the ionic column densities of several of the metal line systems toward Q2206-199. In many cases, we perform hidden component analyses to investigate the presence of hidden saturation (Savage and Sembach 1991). Both the line-profile fitting results and the apparent optical depth method are used to derive column densities.

The hidden component analysis and apparent optical depth method may be summarized in the following manner. One first calculates the apparent ionic column density for each pixel, $N_a(v)$, according to the following equation:

$$N_a(v) = \frac{m_e c \tau_a(v)}{\pi e^2 f \lambda}, \quad (1)$$

where $\tau_a(v) = \ln[I_i(v)/I_a(v)]$, f is the oscillator strength, λ is the rest wavelength, and I_i and I_a are the incident and measured intensity. One then compares $N_a(v)$ profiles from multiple transitions of the same ion to investigate line saturation. Because $\tau_a(v)$ underestimates the true optical depth of strong, unresolved transitions, the inferred $N_a(v)$ will be smaller than for optically thin, weaker transitions. This comparison analysis is termed a hidden component analysis. Additionally, one may sum the $N_a(v)$ profile over velocity space to derive a total ionic column density. This procedure is termed the apparent optical depth method.

4.1. Damped Ly α System at $z = 1.920$

In this section, we perform a comprehensive analysis of the ionic column densities for the damped Ly α system at $z = 1.920$. We first perform a hidden component analysis to investigate the likelihood of hidden line saturation. We then calculate the ionic column densities and 1σ errors and finally make a quantitative evaluation of the effect of hidden saturation in the Ni II and Cr II profiles.

4.1.1. Hidden Component Analysis

Figure 11 plots $N_a(v)$ for the Ni II 1709, 1741, 1751 transitions of the damped Ly α system at $z = 1.920$. The only feature where the $N_a(v)$ curves diverge substantially is at $v = 65 \text{ km s}^{-1}$. Here the strong Ni II 1741 profile depth is significantly smaller than those of the other two weaker transitions. It is possible that there are at least two very narrow

components ($b < 5 \text{ km s}^{-1}$) in this region which are blended in the Ni II 1741 profile. This is an example of hidden saturation, albeit a rather minimal case.

The hidden component analysis of the Cr II 2056, 2062, 2066 transitions is presented in Figure 12. There is a clear indication of hidden saturation in the bluest feature, where the weaker transition (Cr II 2066) dominates. There is also a hint of hidden saturation in the feature at $v = 58 \text{ km s}^{-1}$ corresponding to the hidden saturation observed in the Ni II analysis. The dominant feature at this velocity, though, is the blending apparent in the Cr II 2062 profile due to absorption from Zn II 2062. The divergence between the Cr II profiles at $v \approx 130 \text{ km s}^{-1}$ is also due to absorption from Zn II 2062. Given the results of the two hidden component analyses, we consider the low-ion profiles to be essentially free of hidden saturation with minor exceptions. In order to quantify the effects of hidden saturation on the ionic column densities of these two ions we proceed to implement a correction technique described by Savage and Sembach (1991).

4.1.2. Corrections for Hidden Saturation

As the hidden component analyses of Ni II and Cr II suggest, there is minor hidden saturation evident in several of the low-ion profiles. In order to evaluate the error associated with this saturation, we use the correction technique proposed by Savage and Sembach (1991). We choose to focus on the Cr II saturation because the relative oscillator strengths ($f_{2056} : f_{2066} \approx 2 : 1$) correspond very closely to the analysis by Savage and Sembach (1991). Adopting their notation, express the corrected column density N_a^c as

$$\log N_a^c = \log N_a^{n-1} + \Delta \log N_a^{n-1} \quad (2)$$

where N_a^{n-1} is the column density of the weaker transition, $\Delta \log N_a^{n-1}$ is derived numerically from the difference between $\log N_a^{n-1}$ and $\log N_a^n$, and N_a^n is the column density of the stronger transition³. Using their results (Table 4; Savage and Sembach 1991) and our Cr II measurements ($\log N_a^{n-1} = 13.681$, $\log N_a^n = 13.628$), we find $\Delta \log N_a^{n-1} = 0.053$ implying $\log N_a^c = 13.735$. Thus the hidden saturation in Cr II may lead to an underestimate of the true column density, but by only ≈ 0.05 dex. Note that the Ni II 1741, 1751 measurements ($\log N_a^{n-1} = 13.911$, $\log N_a^n = 13.859$, $\Delta \log N_a^{n-1} = 0.052$) give very similar results. This effect is on the order of the error associated with measuring the column densities and is

³ Hence n denotes the multiple transitions of an ion with increasing n denoting larger f values.

therefore not important. In short, we do not expect abundances inferred from our ionic column densities to suffer significantly from hidden saturation.

4.1.3. Ionic Column Densities and Errors

The measured ionic column densities and 1σ errors for Fe^+ , Ni^+ , Si^+ , Cr^+ , and Zn^+ are listed in Table 10 as measured by both the apparent optical depth (column 2) and line profile fitting (column 3) methods. For the line profile method, we summed the column densities of the individual components of each transition and calculated the 1σ error in the total value with standard least squares techniques. The errors derived for the apparent optical depth method are derived solely from Poisson statistics and are systematically lower than the VPFIT solutions. We believe Poisson statistics alone underestimates the ‘true’ error and therefore adopt the VPFIT error in all cases where VPFIT solutions were obtained. The adopted value for the ionic column density is determined by averaging the measurements from the two methods with the exception of Ni^+ and Cr^+ which have been corrected by the techniques discussed in the previous subsection. Note that in every case the two methods yield nearly the same value, further indicating a lack of significant hidden saturation.

Table 10 also gives the ionic column densities for the s-process transition Cu II 1358, e-process transition Ge II 1602, and Ti II 1910 transitions. As these transitions are very weak, we use the linear curve of growth to infer column densities from the measured rest-frame equivalent widths. The rest frame equivalent widths are: $W(\text{Cu}^+) = 0.0526 \pm 0.0082$, $W(\text{Ge}^+) = 0.0081 \pm 0.0028$, and $W(\text{Ti}^+) = 0.0348 \pm 0.0032$. The ionic column densities for Cu^+ and Ge^+ are derived trivially from the rest frame equivalent width. The Ge^+ column density is reported as 3σ upper limit. The Cu II transition is detected at the 6σ level, but this may be an artifact of the very poor SNR at 3960 Å. The equivalent width for the Ti^+ , however, results from the blend of the two transitions. As the transitions are very weak, we can derive a column density for Ti^+ assuming line blending does not adversely effect the equivalent width (i.e. $W_{tot} = W_{1910}^a + W_{1910}^b$). Using the f values listed in Table 4, we find $\log N(\text{Ti}^+) = 12.807 \pm 0.038$. This represents the first confident ($> 5\sigma$) detection of Ti in a QSO absorption system.

4.2. Damped Ly α System at $z = 2.076$

Unlike the damped system at $z = 1.920$, there are no multiple transitions of any ion in the $z = 2.076$ damped Ly α system. Thus we cannot derive any information regarding hidden saturation. However, given the very low metallicity of the system and the correspondingly weak absorption observed, we do not expect significant hidden saturation effects.

Table 11 presents the ionic column densities of Si $^+$, Fe $^+$, Al $^+$, Si $^{+3}$ and C $^{+3}$ as derived from profile fitting and apparent optical depth methods. Similar to the analysis of the $z = 1.920$ system, we adopt a final value from a weighted average of the two measurements and adopt the VPFIT error. Also included in Table 11 are upper limit measurements for the column density of Ni II 1751 (Ni II 1741 is between orders), Cr II 2056, and Zn II 2026 derived from both the rest-frame equivalent width (assuming the linear curve of growth) and the apparent optical depth method. The measured rest-frame equivalent widths are: $W(\text{Ni}^+) = -0.0009 \pm 0.0012$, $W(\text{Cr}^+) = 0.0052 \pm 0.0014$ and $W(\text{Zn}^+) = 0.0028 \pm 0.0013$. The negative equivalent width value for Ni II 1751 is due to continuum error and is consistent with a null detection. The column densities for Ni II and Zn II are reported as 3σ upper limits while Cr II 2056 was detected at the 3σ level. It is very possible, however, that the Cr II detection is the result of error due to continuum fitting or poor sky subtraction.

4.3. Mg II Systems

4.3.1. $z = 0.752$

Because of significant line saturation in the Mg II system at $z = 0.752$ (Figure 6), the line profile fitting method was unsuccessful. Therefore, we obtained column densities for this system from the profiles which are unsaturated only with the apparent optical depth method. These results are listed in Table 12. A discrepancy exists in the Mn II results (Mn II 2576 has a significantly higher value) which may be due to errors in the oscillator strengths or possibly an unidentified blend. Recalling Mn II 2606 is blended with Fe II 2344 from the MgII system at $z = 0.948$, we adopt a final value by averaging the column densities for Mn II 2576 and Mn II 2594. Figure 13 is a plot of $N_a(v)$ for the Ti II transitions. Because these are very weak transitions, the analysis is not sensitive, but there is moderate evidence for hidden saturation at -20 km s^{-1} . The values for the total column densities from the apparent optical depth method all yield the same value within error and therefore the effect of hidden saturation is minimal. We adopt a Ti II column density for this system by averaging the three values weighted by their respective errors.

4.3.2. $z = 0.948$

Table 13 lists the ionic column densities for the two clouds associated with the Mg II system at $z = 0.948$. There is a significant difference between the column density for Mg II as measured by the two methods. It is very likely hidden saturation may explain the majority of this difference. There is also a minor discrepancy between the column densities measured for the Fe II transitions which again may be due to hidden saturation, but also could be a result of continuum error. For both Fe II and Mg II we suggest adopting the VPFIT values as the VPFIT package does correct for instrumental smearing.

4.3.3. $z = 1.017$

The ionic column densities for Fe^+ , Mg^0 and Mn^+ derived from the apparent optical depth and line profile fitting methods are presented in Table 14. Similar to the $z = 0.948$ system, there is some evidence for hidden saturation in the Fe II profiles (i.e. the weaker Fe II 2374 transition has the highest apparent optical depth ionic column density). We choose to adopt the VPFIT values for the same reasons as above. Note that applying the correction procedure outlined in §4.1.2 yields nearly the VPFIT values.

5. ABUNDANCES

This section presents and discusses the abundance measurements for the two damped Ly α systems based on the ionic column densities of §4. Given the very large neutral Hydrogen column densities observed, we assume the ionized fraction of Hydrogen is insignificant (Prochaska and Wolfe 1996a) and that the metals are predominantly singly ionized (Prochaska and Wolfe 1996a, Lu et al. 1995). Therefore the abundances are derived from the ionic column densities of H^0 , Ti^+ , Fe^+ , Si^+ , Cr^+ , Ni^+ , and Zn^+ without ionization corrections.

As a qualitative check, we can compare the Al III 1854 and low-ion line profiles, where a relative overabundance of Al III may suggest an ionized region. With the exception of the velocity region near $v \approx 25 \text{ km s}^{-1}$, the profiles trace one another closely. There is a possibility that the gas is in a higher ionization state at this velocity, but lacking an unsaturated Al II profile it is difficult to quantify the effect on the abundances. As such, we choose to ignore ionization corrections since this one velocity region would have at most only a minor effect on our results.

5.1. Damped Ly α System at $z = 1.920$

5.1.1. Results

The logarithmic column density $\log[N(X)]$, and the logarithmic abundance of element X relative to Hydrogen normalized to solar abundances, $[X/H] \equiv \log[N(X)/N(H)] - \log[N(X)/N(H)]_{\odot}$, for the damped Ly α system at $z=1.920$ are listed in Table 15. The abundances for this system are derived assuming $N(H) = 4.5 \pm 0.8 \times 10^{20} \text{ cm}^{-2}$ (Pettini et al. 1994) and standard solar abundances (Anders & Grevesse 1989). Given the quality of the Keck data, the error in $N(H)$ dominates the error in the abundances. Therefore measurements of the relative abundances of different elements will have substantially smaller errors associated with them. This system has the highest metallicity that we have analyzed for a damped Ly α system with $[Zn/H] = -0.374 \pm 0.097$ and $[Fe/H] = -0.705 \pm 0.097$. We report both Zn and Fe as indicators of metallicity given the results of recent studies (see Lu et al. 1996a, Prochaska and Wolfe 1996a). Note that our value for Zn is consistent with the lower limit presented by Pettini et al. (1994).

5.1.2. Relative Abundances and Dust

Figure 14 plots the abundance data versus condensation temperatures, T_C . Also shown in the figure are the corresponding values for the sightline to ζ Oph in the ISM where the underabundance of metals with respect solar abundances is assumed the result of depletion onto dust grains. Comparing the damped Ly α data with the ISM values reveals minimal evidence for a dust-like pattern, in which Fe and Ni are underabundant relative to Zn. The equality of the Zn and Si abundance argues against this interpretation since Si is underabundant relative to Zn in the Galaxy. Moreover, the abundance pattern we observe in the damped Ly α data, in particular $[Ni/Fe]$, $[Si/Fe]$ and $[Cr/Fe]$, resembles the pattern detected in halo stars in the Galaxy which are explained in terms of nucleosynthetic yields produced by type II supernovae (Lu, Sargent, & Barlow 1995, Lu et al. 1996a, Lu et al. 1996b, Prochaska and Wolfe 1996a). The Lu et al. interpretation has one serious difficulty. In all damped Ly α systems $[Zn/Fe] > 0$, whereas $[Zn/Fe] \approx 0$ for stars with $-3 < [Fe/H] < 0$ (Snedden et al. 1991).

Lu et al. (1996a) have stressed the importance of the relative abundance of Mn to Fe as a strong indicator of the presence of dust in damped Ly α systems. For a large range of metallicities $[Mn/Fe] > 0$ in the ISM, whereas Lu et al. (1996a) find $[Mn/Fe] \leq 0$ for all of the damped Ly α systems they have analyzed. In turn, they argue the abundance ratios of damped Ly α systems are not consistent with dust depletion while they are consistent with

the yields from type II supernovae. We can apply similar arguments to the $[\text{Ti}/\text{Fe}]$ ratio where depletion in the ISM implies $[\text{Ti}/\text{Fe}] < 0$ over a wide range of metallicities. For the damped $\text{Ly}\alpha$ system at $z = 1.920$ we find $[\text{Ti}/\text{Fe}] = -0.071 \pm 0.069$, which is consistent (at the 1σ level) with no dust depletion. Furthermore the $[\text{Ti}/\text{Fe}]$ ratio is consistent with the value observed in higher metallicity Galactic stars (Wheeler et al. 1989).

5.1.3. *Relative Abundances Variations and Dust*

Figure 15 is a plot of the abundance of Si, Fe, Ni, and Cr relative to Zn in velocity space assuming solar abundances. The small points represent a 5 pixel average of the relative abundance at the given velocity, while the larger points represent relative abundances over the velocity regions designated by the dashed vertical lines. There are several systematic features resulting from the shape of the Zn II profile which need to be addressed. First, the spike at $v = 10 \text{ km s}^{-1}$ in each plot is most likely due to a sky emission line that was poorly subtracted from the Zn II profile. Secondly, the slight dip at $v = 50 \text{ km s}^{-1}$ is due to a blend of Zn II 2026 with Mg I 2026. Finally, the region at $v > 125 \text{ km s}^{-1}$ is dominated by noise as all the profiles show essentially no absorption.

Examining the averaged values, one notes the relative abundances remain nearly constant over the entire velocity interval with only small deviations primarily due to the systematic effects addressed above. Quantitatively, the variation is on the order of ≈ 0.2 dex. Using identical techniques to those presented in Prochaska and Wolfe 1996a, we find variations of the hydrogen volume density n_H are no larger than ≈ 0.5 dex if ISM-like dust is present in this system. As discussed in Prochaska and Wolfe 1996a, we therefore conclude either: (1) there is an absence of grains with properties similar to dust in the ISM or (2) the input of shocks driven by Supernovae in this system is considerably weaker than that in the ISM. Furthermore, recent studies of metal abundances in the ISM (Spitzer and Fitzpatrick 1993, Spitzer and Fitzpatrick 1995) have indicated relative abundance (depletion) variations of nearly 1.0 dex for Ni and Fe with respect to S. Our data does not exhibit this same trend where we consider Zn, a relatively undepleted element, instead of S. Therefore, we contend the lack of abundance variations in this system suggests the lack of a significant amount of ISM-like dust.

5.2. Damped Ly α System at $z = 2.076$

Table 16 lists the column density and logarithmic abundance of the metals associated with the damped Ly α system at $z = 2.076$. The values for the Ni and Zn abundances represent 3σ upper limits. Because the Cr II transition is such a marginal detection (i.e. the transition is dominated by noise), we believe its abundance may be significantly lower. In any case, this system is very metal poor, exhibiting the lowest metallicity ($[\text{Zn}/\text{H}] < -1.745$, $[\text{Fe}/\text{H}] = -2.621 \pm 0.071$) we have measured for a damped system thus far. The abundance measurements of Zn and Cr are a significant improvement over all previous work. In the case of Zn, for example, we have lowered the previous upper limit by nearly 1 dex.

Figure 16 is a plot of the abundance data as a function of condensation temperature. Note that all of the abundances are consistent with an overall metallicity $[\text{Zn}/\text{H}] < -1.745$. Given the small number of metal transitions analyzed here and the absence of a positive detection of Zn, it is very difficult to comment on the likelihood of dust in this system.

5.3. Damped? Ly α System at $z = 0.752$

If we assume solar abundances relative to Hydrogen and assume the overall metallicity of this system is lower than solar (i.e. $[\text{Zn}/\text{H}], [\text{Fe}/\text{H}] < 0.0$ dex), the Fe^+ , Mn^+ and Ti^+ ionic column densities of the $z = 0.752$ damped system imply $\log N(\text{HI}) > 19.06$, 19.00 , and 19.37 respectively. Therefore, we believe it is very likely that this system is in fact a damped Ly α system. As discussed in §5.1.2, the $[\text{Mn}/\text{Fe}]$ ratio may be a strong indicator of the presence (or lack thereof) of dust grains in damped Ly α systems. For this system, we find $[\text{Mn}/\text{Fe}] = -0.099 \pm 0.061$ which further supports the results of Lu et al. (1996a; see §5.1.2). Comparing the relative abundance of Ti to Fe, we find $[\text{Ti}/\text{Fe}] = 0.269 \pm 0.042$ which also is inconsistent with dust depletion, where $[\text{Ti}/\text{Fe}] < 0$ in dust depleted regions within the ISM. Also, the $[\text{Ti}/\text{Fe}]$ ratio is observed to increase with decreasing metallicity in Galactic stars (Wheeler et al. 1989), owing to the fact that Ti is an even- Z , α -element. Because the value of $[\text{Ti}/\text{Fe}]$ for the $z = 0.752$ system is consistent with the values of Galactic halo stars, we contend this abundance ratio is consistent with the Lu et al. interpretation and inconsistent with dust depletion.

6. KINEMATICS

6.1. Damped Ly α System at $z = 1.920$

In this subsection we discuss the kinematics of the damped Ly α system at $z=1.920$. We stress the observed differences between the high and low-ion profiles and compare the velocity profiles of the $z=1.920$ system with several other damped Ly α systems.

6.1.1. Comparison of the Low and High Ion Profiles

Although the shape of the high-ion profiles (C IV and Si IV) are dominated by line saturation, the profiles clearly differ from the low-ion profiles. For instance, the blue wing of the high-ion profile is smoother and extends further than the low-ion blue wing. In addition, there is significant absorption at several velocities in the high-ion velocity profile (e.g. $v = 20 \text{ km s}^{-1}$) not observed in the low-ion transitions. Finally, the velocity interval for the high ions extends much further redward. Given these observations, we contend that the low and high ions are to a large degree kinematically disjoint.

This characteristic has been observed in other damped Ly α systems (Wolfe et al. 1994, Prochaska and Wolfe 1996a) we investigated with HIRES. It is very possible that the high-ion absorption may be from different regions within the system. Specifically, the high-ion absorption may be due to hotter halo gas while the low ions may predominate in the inner disk. The large widths of the C IV profiles indicate this may be the case.

6.1.2. Comparison with Other Damped Ly α Systems

Our previous studies on the kinematics of damped Ly α systems have revealed a systematic asymmetry (termed 'edge-leading asymmetry') in the velocity profiles. In short, the low-ion profiles of the damped Ly α system at $z = 2.309$ toward PHL 957 and at $z = 2.462$ toward Q0201+365 have the strongest absorption feature at one edge of the velocity interval and exhibit a decline in absorption toward the other edge. We believe this effect can be explained by passage of the line of sight through a thick, rapidly rotating disk ($v_{rot} \sim 200 \text{ km s}^{-1}$) in which the density of absorbing clouds decreases with radius and height from midplane (Wolfe 1995).

A similar effect (albeit less dramatic) is seen in the low-ion profiles of the $z = 1.920$ damped Ly α system. The strongest feature lies at the blue edge of the velocity interval with declining absorption toward the red. By contrast with the PHL 957 and Q0201+365 damped systems this system shows a lack of absorption over a significant velocity interval

($\Delta v \approx 40 \text{ km s}^{-1}$) between the two strongest features. Beyond the second feature ($v > 50 \text{ km s}^{-1}$) the profile clearly possesses the edge-leading asymmetry. We consider this profile to be consistent with an edge-leading asymmetry, but note that its shape is not as suggestive as the majority of the other cases. It is interesting to note that the Al III profile, which is not identified as either a low or high ion, exhibits a very clear edge-leading asymmetry.

6.2. Damped Ly α System at $z = 2.076$

6.2.1. Comparison of the Low and High Ion Profiles

Similar to the $z = 1.920$ system, the high-ion profiles of the $z = 2.076$ damped Ly α system exhibit absorption over a wider velocity interval and at significantly different velocities than the low-ion profiles. However, unlike the $z = 1.920$ system the Si IV and C IV profiles do not trace one another very closely. This may be predominantly due to the lower metallicity or different ionization conditions.

6.2.2. Comparison with Other Damped Ly α Systems

Given the very low metallicity and correspondingly weak absorption features of the $z = 2.076$ system, it is difficult to compare its kinematics with other damped Ly α systems. The $z = 2.076$ system does not show the edge-leading asymmetry and is in fact a very symmetric profile. In addition, the low and high-ion profiles span the smallest velocity intervals observed thus far for a damped Ly α system. At the same time, however, these characteristics are easily accommodated within the thick rotating disk model. The line-of-sight may be penetrating the disk nearly face-on or may be at several scale lengths from the center of the disk thereby sampling a very small portion of the circular velocity field. A future paper (Prochaska and Wolfe 1996b) will investigate the likelihood of such an occurrence.

7. SUMMARY AND CONCLUSIONS

We have presented high SNR HIRES spectra of the QSO Q2206-199 and have identified over 85% of the features redward of Ly α emission (Table 3). We have analyzed 8 metal line systems in depth and summarize the results as follows.

- (1) Although there is an indication of hidden line saturation in the Ni II and Cr

II transitions of the $z = 1.920$ damped Ly α system, our analysis predicts the effect on the measured abundances is smaller than the 1σ Poisson statistical errors. Therefore we confidently present abundance measurements of Fe, Cr, Ni, Si, Ti and Zn relative to solar abundances where the majority of error lies in the measurement of $N(\text{HI})$: $[\text{Fe}/\text{H}] = -0.705 \pm 0.097$, $[\text{Cr}/\text{H}] = -0.580 \pm 0.100$, $[\text{Si}/\text{H}] = -0.402 \pm 0.098$, $[\text{Ni}/\text{H}] = -1.012 \pm 0.095$, $[\text{Ti}/\text{H}] = -0.776 \pm 0.081$ and $[\text{Zn}/\text{H}] = -0.379 \pm 0.097$. The measurement of Ti is the first confident ($> 5\sigma$) detection in a QSO absorption line system. In addition, we place a 3σ upper limit on the Ge abundance ($[\text{Ge}/\text{H}] < 0.147$) and report a tentative detection of $[\text{Cu}/\text{H}] = 0.039 \pm 0.102$ in this system.

(2) We have performed several analyses to test for the presence of dust grains in the $z = 1.920$ damped Ly α system. Plots of abundances relative to solar versus condensation temperature exhibit little evidence for the presence of dust grains when compared to similar plots for the sightline to ζ Oph. The abundance pattern of the damped system does follow the ζ Oph data in that Zn is overabundant with respect to Ni, Fe and possibly Cr, but the differences are comparatively small. In addition, $[\text{Si}/\text{H}] \approx [\text{Zn}/\text{H}]$ in the damped system which clearly contradicts the ISM data. We contend this analysis is consistent both with the existence of ISM-like dust at a level significantly below that of the sightline to ζ Oph as well as the abundance patterns of halo stars which have been enriched by type II supernovae. Furthermore, we measure $[\text{Ti}/\text{Fe}] \approx 0$ which is consistent with no dust depletion.

We have searched for abundance variations of Fe, Si, Cr and Ni relative to Zn over the velocity interval spanning the low-ion profiles. We observe very small variations (≈ 0.2 dex) and have used techniques developed in previous work (Prochaska and Wolfe 1996a) to conclude: (a) either the input of shocks driven by supernovae is considerably weaker in this system than that in the ISM or (b) there is a very low level of ISM-like dust grains present in the system.

(3) The abundances of the damped Ly α system at $z = 2.076$ are very low. Analyzing the strong Fe II, Si II and Al II transitions we derived the following abundances: $[\text{Fe}/\text{H}] = -2.621 \pm 0.071$, $[\text{Si}/\text{H}] = -2.225 \pm 0.075$, $[\text{Al}/\text{H}] = -2.727 \pm 0.070$. Even with our excellent resolution and moderately high SNR we could only place upper limits on the abundance of Zn and Ni ($[\text{Zn}/\text{H}] < -1.745$ and $[\text{Ni}/\text{H}] < -2.384$). We report a tentative measurement of Cr, $[\text{Cr}/\text{H}] = -2.00 \pm 0.15$, whose value we question as noise dominates the absorption profile. Lacking abundance data for Zn, we could not perform a detailed dust analysis for this system.

(4) In addition to having widely different metallicities, the $z = 2.076$ and $z = 1.920$ damped Ly α systems exhibit remarkably different kinematic characteristics. The low-ion profiles (expected to trace the kinematics of these predominantly neutral systems) of

the $z = 1.920$ system span $\approx 150 \text{ km s}^{-1}$ in velocity space and are largely asymmetric. Conversely, the low-ion profiles of the $z = 2.076$ system span only 30 km s^{-1} and are highly symmetric. Even given these differences, the two profiles are consistent with the kinematics expected from a thick, fast ($\approx 200 \text{ km s}^{-1}$) rotating disk. The $z = 1.920$ profiles can be explained with a moderately inclined disk, while the $z = 2.076$ profile would be due to a nearly face-on disk (low probability) or a line of sight which penetrated the outer regions of the disk (more likely) where the radius of curvature is small. These ideas will be more fully developed in future work (Wolfe et al. 1996, Prochaska and Wolfe 1996b).

(5) We have investigated a very strong Mg II system at $z = 0.752$. This system shows absorption in the very weak Mn II 2606, 2594, 2576 and Ti II 3073, 3342, and 3384 transitions. Together with the damped Ly α system at $z = 1.920$, this marks the first time Ti has been confidently observed in the IGM. The column densities we derived from these transitions imply a very conservative lower limit to $N(\text{HI})$ of $\log N(\text{HI}) > 19.00$, having assumed solar abundances and no depletion. We believe it is very possible that this is a third damped system toward Q2206–199.

The relative abundance ratios of Mn and Ti to Fe strongly suggest the system does not suffer from dust depletion. Specifically, $[\text{Mn}/\text{Fe}] = -0.099 \pm 0.061$ and $[\text{Ti}/\text{Fe}] = 0.269 \pm 0.042$, whereas in the ISM gas affected by dust depletion has $[\text{Mn}/\text{Fe}] > 0$ and $[\text{Ti}/\text{Fe}] < 0$. These results essentially rule out the possibility of dust depletion and further support the hypothesis of Lu et al. (1996a) that the abundance patterns of damped Ly α systems are characteristic of type II supernovae.

(6) We have identified a C IV system at $z = 2.014$ with a very narrow feature seen in C IV and Si IV absorption. The b values (8.9 km s^{-1} and 5.2 km s^{-1} for C IV and Si IV respectively) suggest a temperature of $4.7 \times 10^4 \text{ K}$. As collisional ionization dominates the production of these ions at $T > 8 \times 10^4 \text{ K}$, we believe collisional ionization is not the dominant process of formation. This marks the first unambiguous evidence for earlier claims (York et al. 1984) of the existence of C IV systems in the IGM formed by a process other than collisional ionization.

The authors would like to thank Bob Carswell for providing the line-profile fitting package VPFIT as well as Tom Barlow for his excellent HIRES data reduction software. AMW and JXP were partially supported by NASA grant NAGW-2119 and NSF grant AST 86-9420443.

UT Date	Exposure Time (s)	Wavelength Coverage (Å)	Resolution (km s ⁻¹)
1994 Sep 15	10800	3940 - 6360	7.2 - 8.0
1994 Sep 30	7200	4140 - 6520	7.4 - 8.0
1994 Oct 1	7900	4140 - 6520	7.2 - 8.0

Table 1: JOURNAL OF OBSERVATIONS

Order	λ_{center} Å	SNR
90	3960	9.7
85	4190	21.8
80	4450	38.7
75	4750	34.7
70	5090	45.4
65	5480	60.8
60	5940	47.1
55	6480	41.4

Table 2: SNR FOR SEVERAL ORDERS

Table 3. ABSORPTION LINE LIST

Order	λ (\AA)	W (\AA)	σ_W	ID	z_{abs}	
90	3946.45	0.0651	0.0118			
	3950.40	0.2511	0.0156			
	3957.38	1.7486	0.0245			
	3960.83	0.0480	0.0085	FeII 2260	0.752	
	3964.61	0.5092	0.0151			
	3968.53	0.0468	0.0082			
	3969.11	0.0537	0.0094			
	3972.20	0.3433	0.0139			
	3974.11	1.6655	0.0207			
	3977.75	1.2153	0.0228			
	3982.86	0.0818	0.0127			
	3984.10	0.5275	0.0271			
	89	3977.82	1.1607	0.0282		
		3984.39	0.4686	0.0222		
3988.39		2.5651	0.0301	Ly-a 1215	2.281	
3992.31		1.4807	0.0268			
3995.72		1.4815	0.0186			
3998.46		0.3567	0.0142			
4001.73		0.4066	0.0179	NiII 1370	1.920	
4005.76		0.2964	0.0084	OI 1302	2.076	
4008.02		1.7333	0.0231			
4012.52		0.1380	0.0079	SiII 1304	2.076	
4015.99		0.1495	0.0136			
4020.97		0.0760	0.0129			
4022.39		0.1318	0.0134			
88		4022.01	0.0957	0.0160		
	4037.14	2.3788	0.0217	Ly-a 1215	2.321	
	4045.66	0.5778	0.0119			
	4047.16	0.0411	0.0081			
	4048.43	0.0628	0.0091			
	4049.37	0.3253	0.0113			
	4052.17	0.1348	0.0113			
	4057.66	0.9004	0.0168			
	4060.77	0.8117	0.0201			
	4068.01	0.0738	0.0107			
	4068.55	0.1006	0.0098			
	4070.42	2.5209	0.0229	SiIV 1393	1.920	
	4073.78	2.3038	0.0268			
	4075.73	0.0634	0.0089			
87	4068.33	0.0995	0.0120			
	4070.42	2.5209	0.0229	SiIV 1393	1.920	
	4073.78	2.3038	0.0268			
	4087.44	0.9204	0.0172			
	4088.90	0.0378	0.0064			
	4089.96	0.1436	0.0110			
	4091.22	0.3615	0.0143			
	4094.65	0.0828	0.0101			
	4097.09	2.6619	0.0196	SiIV 1402	1.920	
	4100.06	0.4152	0.0140			
	4105.10	0.5883	0.0150	CII 1334	2.076	
	4106.79	0.8740	0.0113	FeII 2344	0.752	
	4108.05	0.5139	0.0117			
	4110.05	0.3905	0.0181			
4113.05	2.6078	0.0222				
4115.74	0.2083	0.0131				
4118.29	0.0592	0.0085				
4120.18	0.4861	0.0139				
86	4113.64	2.0268	0.0250			
	4115.84	0.1844	0.0158			
	4120.22	0.4658	0.0143			
	4123.89	2.3905	0.0204			
	4125.89	0.1217	0.0124			
	4127.63	0.0752	0.0102			
	4129.25	0.3551	0.0115			

Table 3—Continued

Order	λ (\AA)	W (\AA)	σ_W	ID	z_{abs}
	4132.64	0.1138	0.0081		
	4135.10	0.0625	0.0067		
	4143.38	0.4809	0.0087		
	4145.27	0.0220	0.0037		
	4152.07	0.1950	0.0065		
	4154.18	0.9786	0.0099		
	4159.77	0.6149	0.0078	FeII 2374	0.752
	4165.60	0.4197	0.0113		
85	4165.69	0.4364	0.0132		
	4172.63	0.1147	0.0071		
	4174.51	1.2104	0.0094	FeII 2382	0.752
	4182.16	0.0274	0.0038		
	4186.41	4.7572	0.0128	Ly-a 1215	2.445
	4192.97	0.0689	0.0054		
	4197.51	0.1836	0.0058		
	4201.35	0.1796	0.0046	SiIV 1393	2.014
	4202.99	0.0152	0.0030		
	4206.27	0.0555	0.0050		
	4206.86	0.0313	0.0040		
	4208.68	1.2575	0.0072		
	4217.03	0.0666	0.0040	MgII 2796	0.508
	4218.43	0.0296	0.0049		
	4219.87	0.0316	0.0053		
84	4217.04	0.0715	0.0041	MgII 2796	0.508
	4218.41	0.0659	0.0062		
	4219.80	0.0537	0.0059		
	4220.69	0.2278	0.0063		
	4226.86	0.1417	0.0053		
	4227.96	0.0717	0.0034	MgII 2803	0.508
	4228.49	0.1481	0.0044	SiIV 1402	2.014
	4231.22	0.3129	0.0068		
	4232.97	0.0416	0.0046		
	4234.16	0.1104	0.0051		
	4237.71	0.1946	0.0056		
	4240.00	0.2172	0.0055		
	4242.73	0.1727	0.0054		
	4245.22	0.1196	0.0046		
	4246.34	0.1254	0.0046		
	4247.80	0.1523	0.0044		
	4248.48	0.0098	0.0018		
	4249.22	0.1844	0.0052	NI 1199	2.542
	4252.45	B ^a		NiII 1454	1.920
	4256.16	2.1368	0.0095		
	4260.37	0.0249	0.0031		
	4261.68	0.8938	0.0059		
	4267.67	0.0890	0.0055	NV 1238	2.445
83	4261.74	0.9095	0.0070		
	4267.56	0.0920	0.0052	NV 1238	2.445
	4269.43	0.0421	0.0047		
	4272.22	0.1943	0.0048	OI 1302?	2.281
	4273.66	0.0156	0.0026		
	4274.53	0.0237	0.0028		
	4276.33	1.4103	0.0074		
	4279.40	0.1920	0.0046		
	4285.82	B ^a		NiII 1467	1.920
	4288.65	B ^a		Si IV 1392	2.076
	4293.15	0.0666	0.0033		
	4296.63	2.6738	0.0076		
	4300.57	0.1345	0.0040		
	4302.55	0.1181	0.0038		
	4306.60	2.6804	0.0051	Ly-a 1215	2.542
	4315.31	0.0850	0.0033	SiIV 1402	2.076
	4319.76	0.5776	0.0046		
82	4315.28	0.0958	0.0042	SiIV 1402	2.076
	4319.81	0.5773	0.0047		

Table 3—Continued

Order	λ (\AA)	W (\AA)	σ_W	ID	z_{abs}
	4320.90	0.0156	0.0026		
	4322.33	0.1549	0.0041		
	4327.50	0.3559	0.0045		
	4329.53	0.0106	0.0020		
	4331.57	0.5283	0.0050		
	4334.76	0.2405	0.0038		
	4357.98	0.0823	0.0022	SiIV 1393	2.126
81	4359.99	0.0520	0.0027	SiIV 1393	2.128
	4386.17	0.0617	0.0026	SiIV 1402	2.126
80	4388.29	0.0260	0.0025	SiIV 1402	2.128
	4458.75	2.8803	0.0053	SiII 1526	1.920
79					
	4512.28	0.0443	0.0029		
	4514.45	0.1441	0.0052	MnII 2576	0.752
	4521.84	3.3834	0.0084	C IV 1548	1.920
	4529.77	B ^a		C IV 1550	1.920
	4538.29	0.0224	0.0033		
78					
	4544.98	0.0642	0.0053	MnII 2594	0.752
	4555.25	1.1287	0.0051	FeII 2600	0.752
	4560.36	0.0174	0.0025	FeII 2260	1.017
	4566.44	B ^a		MnII 2606	0.752
	4572.29	S ^b		SKY	
77					
	4604.05	0.0330	0.0037	CIV 1548	1.974
	4611.76	0.0206	0.0032	CIV 1550	1.974
	4641.08	0.0146	0.0022	FeII 2382	0.948
	4642.48	0.0400	0.0028	FeII 2382	0.948
76					
	4665.04	0.0986	0.0052	CIV 1548	2.014
	4666.98	0.5255	0.0064	CIV 1548	2.014
	4672.69	0.0517	0.0039	CIV 1550	2.014
	4674.83	0.3407	0.0057	CIV 1550	2.014
	4697.38	B ^a		FeII 1608	1.920
	4705.00	0.1657	0.0066	FeII 1611	1.920
75					
	4728.23	0.8145	0.0064	FeII 2344	1.017
	4731.12	0.0114	0.0022	FeII 2344	1.018
	4762.81	0.4712	0.0049	C IV 1548	2.076
	4770.56	0.2718	0.0041	C IV 1550	2.076
74					
	4789.24	0.4111	0.0066	FeII 2374	1.017
	4805.90	1.1945	0.0052	FeII 2382	1.017
	4808.90	0.0340	0.0024	FeII 2382	1.018
	4840.87	0.0764	0.0032	CIV 1548	2.128
	4843.10	0.1480	0.0048	CIV 1548	2.128
	4843.84	0.0265	0.0039	CIV 1548 ?	2.129
	4844.75	0.1160	0.0053	CIV 1548 ?	2.129
73					
	4848.88	0.0373	0.0035	CIV 1550	2.128
	4851.20	0.0775	0.0039	CIV 1550	2.128
	4852.74	0.0473	0.0049	CIV 1550	2.129
	4879.45	3.1863	0.0057	AlII 1670	1.920
	4888.16	0.0332	0.0031		
	4899.00	1.5708	0.0052	MgII 2796	0.752
	4911.72	1.4135	0.0055	MgII 2803	0.752
72					
	4912.26	0.7060	0.0056	MgII 2803	0.752
	4947.94	0.0749	0.0024	FeII 1608	2.076
	4969.58	0.1531	0.0032	CIV 1548	2.210
	4973.91	0.0141	0.0024	NiII 1703	1.920
	4977.79	0.0957	0.0032	CIV 1550	2.210
71					
	4992.82	0.3562	0.0068	NiII 1709	1.920
	4998.16	0.4040	0.0050	Mg I 2852	0.752
70					
	5066.05	0.0417	0.0030	FeII 2600	0.948

Table 3—Continued

Order	λ (\AA)	W (\AA)	σ_W	ID	z_{abs}
	5079.82	0.1466	0.0029	CIV 1548	2.281
	5086.17	0.5020	0.0064	NiII 1741	1.920
	5088.39	0.1195	0.0034	CIV 1550	2.281
	5097.09	0.0114	0.0020		
69	5116.46	0.3559	0.0071	NiII 1751	1.920
	5139.71	0.1553	0.0035	AlII 1670	2.076
	5141.45	0.1865	0.0068	CIV 1548	2.321
	5150.00	0.0679	0.0063	CIV 1550	2.321
68	5197.93	0.0231	0.0040	MnII 2576	1.017
	5217.15	0.7297	0.0059	FeII 2586	1.017
	5233.60	0.0226	0.0029	MnII 2594	1.017
	5244.40	1.2150	0.0046	FeII 2600	1.017
	5247.70	0.0219	0.0020	FeII 2600	1.018
	5251.41	0.0148	0.0025		
	5257.58	0.0188	0.0029	MnII 2606	1.017
	5270.17	0.0177	0.0028		
67	5280.20	0.9075	0.0093	SiII 1808	1.920
	5333.72	0.1860	0.0040	CIV 1548	2.445
	5342.63	0.0982	0.0042	CIV 1550	2.445
66	5385	0.0210	0.0038	TiII 3073	0.752
	5394.39	0.0119	0.0021		
	5410.96	0.0150	0.0019		
	5411.26	0.0134	0.0016		
	5416.90	2.0526	0.0073	AlIII 1854	1.920
65	5441.40	0.4677	0.0055	AlIII 1862	1.920
	5446.74	0.1397	0.0034	MgII 2796	0.948
	5448.36	0.3411	0.0028	MgII 2796	0.948
	5460.73	0.0932	0.0025	MgII 2803	0.948
	5462.30	0.2674	0.0026	MgII 2803	0.948
	5473.29	0.0125	0.0017		
	5483.81	0.0602	0.0026	CIV 1548	2.542
	5491.80	B ^a		CIV 1550	2.542
	5492.87	0.0352	0.0024	CIV 1550	2.542
64	5556.92	0.0131	0.0016	MgI 2852	0.948
	5575.17	0.0209	0.0024	TiII 1910a	1.920
	5578.96	0.0174	0.0024	TiII 1910a	1.920
	5580.05	0.0286	0.0026	TiII 1910b	1.920
	5581.14	0.0231	0.0027	TiII 1910b	1.920
63	5640.23	2.0372	0.0055	MgII 2796	1.017
	5643.64	0.0907	0.0025	MgII 2796	1.018
	5654.54	1.7992	0.0046	MgII 2803	1.017
	5658.10	0.0528	0.0021	MgII 2803	1.018
	5660.88	0.0144	0.0017	TiII 3230	0.752
	5680	0.0590	0.0046	TiII 3242	0.752
62	5749.35	0.0122	0.0020		
	5754.59	0.3604	0.0049	MgI 2852	1.017
61					
60	5897.44	S ^b		Sky Abs	
	5901.23	S ^b		Sky Abs	
	5902.81	S ^b		Sky Abs	
	5910.25	S ^b		Sky Abs	
	5917.00	0.3952	0.0069	ZnII 2026	1.920
	5919.57	S ^b		Sky Abs	
	5920.27	S ^b		Sky Abs	
	5923.73	S ^b		Sky Abs	
	5925.02	S ^b		Sky Abs	
	5930	0.0963	0.0045	TiII 3384	0.752
	5933.25	S ^b		Sky Abs	
	5942.36	S ^b		Sky Abs	
	5942.90	S ^b		Sky Abs	

Table 3—Continued

Order	λ (\AA)	W (\AA)	σ_W	ID	z_{abs}
	5943.77	S ^b		Sky Abs	
	5950.38	S ^b		Sky Abs	
	5972.59	S ^b		Sky Abs	
59	6005.24	0.4274	0.0072	CrII 2056	1.920
	6023.17	B ^a		CrII 2062	1.920
	6034.29	0.2268	0.0059	CrII 2066	1.920
58					
57					
	6276 –	S ^b		Sky Abs	
56					
55					
	6439.81	0.2705	0.0047		
	6476.38	S ^b		Sky Abs	
	6477.06	S ^b		Sky Abs	
	6481.37	S ^b		Sky Abs	
	6484.54	S ^b		Sky Abs	
	6494.24	S ^b		Sky Abs	
	6497.18	S ^b		Sky Abs	
	6517.85	S ^b		Sky Abs	

^a Line blending

^b Night-sky absorption or emission features

Table 4. METAL TRANSITIONS

Transition	λ_{rest} (\AA)	f
SiIV 1393	1393.755	0.528
SnII 1400	1400.400	0.71
SiIV 1402	1402.770	0.262
GaII 1414	1414.402	1.8
SiII 1526	1526.707	0.2303
CIV 1548	1548.195	0.1908
CIV 1550	1550.770	0.09522
GeII 1602	1602.4863	0.135
FeII 1608	1608.4449	0.05545
FeII 1611	1611.2004	0.001020
AlII 1670	1670.7874	1.88
PbII 1682	1682.15	0.156
NiII 1741	1741.549	0.1035
NiII 1751	1751.910	0.0638
SiII 1808	1808.0126	0.00218
AlIII 1854	1854.716	0.539
AlIII 1862	1862.790	0.268
TiII 1910a	1910.6	0.0975
TiII 1910b	1910.97	0.0706
ZnII 2026	2026.136	0.515
CrII 2056	2056.254	0.1403
CrII 2062	2062.234	0.1049
ZnII 2062	2062.664	0.2529
FeII 2344	2344.214	0.1097
FeII 2374	2374.4612	0.02818
FeII 2382	2382.765	0.3006
FeII 2600	2600.1729	0.2239
MgII 2796	2796.352	0.6123
MgII 2803	2803.531	0.3054
TiII 3073	3073.877	0.1091
TiII 3230	3230.131	0.05861
TiII 3242	3242.929	0.1832
TiII 3384	3384.740	0.3401

Table 5a. FIT FOR $z=1.920$ – LOW IONS

Comp	z	σ_z $\times 10^{-5}$	b (km s^{-1})	σ_b (km s^{-1})	ION	$\log N$ (cm^{-2})	$\sigma_{\log N}$ (cm^{-2})
1	1.919912	4.4	10.28	2.71	Si ⁺	14.81	0.23
					Fe ⁺	14.35	0.27
					Ni ⁺	12.77	0.25
					Cr ⁺	12.70	0.23
					Zn ⁺	11.89	0.24
2	1.919991	0.2	5.04	0.68	Si ⁺	15.00	0.14
					Fe ⁺	14.65	0.12
					Ni ⁺	13.14	0.10
					Cr ⁺	12.84	0.15
					Zn ⁺	12.09	0.14
3	1.920169	0.8	9.66	1.62	Mg ⁰	12.00	0.17
					Si ⁺	14.72	0.07
					Fe ⁺	14.30	0.12
					Ni ⁺	12.77	0.07
					Cr ⁺	12.37	0.10
4	1.920407	1.7	11.76	2.00	Zn ⁺	11.51	0.12
					Si ⁺	14.97	0.11
					Fe ⁺	14.68	0.11
					Ni ⁺	13.02	0.12
					Cr ⁺	12.83	0.12
5	1.920566	0.5	3.93	1.33	Zn ⁺	12.16	0.11
					Si ⁺	14.71	0.14
					Fe ⁺	14.23	0.20
					Ni ⁺	12.72	0.18
					Cr ⁺	12.53	0.19
6	1.920660	0.5	1.51	1.93	Zn ⁺	11.90	0.13
					Si ⁺	14.70	0.34
					Fe ⁺	14.37	0.12
					Ni ⁺	12.50	0.13
					Cr ⁺	12.31	0.15
7	1.920706	3.8	17.91	4.63	Zn ⁺	11.64	0.11
					Si ⁺	15.16	0.16
					Fe ⁺	14.77	0.19
					Ni ⁺	13.27	0.16
					Cr ⁺	12.66	0.12
8	1.921033	3.0	19.72	2.85	Zn ⁺	12.29	0.16
					Si ⁺	14.85	0.10
					Fe ⁺	14.61	0.11
					Ni ⁺	13.06	0.09
					Cr ⁺	13.10	0.15
9	1.921373	0.8	10.77	2.97	Zn ⁺	12.06	0.09
					Si ⁺	14.11	0.12
					Fe ⁺	13.94	0.27
					Ni ⁺	12.11	0.15
					Cr ⁺	11.64	0.31
					Zn ⁺	10.83	0.48

Comp	z	σ_z ($\times 10^{-5}$)	b (km s^{-1})	σ_b (km s^{-1})	Ion	$\log N$ (cm^{-2})	$\sigma_{\log N}$ (cm^{-2})
1	1.919534	0.6	8.56	0.76	Al ⁺⁺	12.22	0.03
2	1.919733	0.7	9.27	1.66	Al ⁺⁺	12.17	0.06
3	1.919993	0.3	10.02	0.34	Al ⁺⁺	13.35	0.01
4	1.920245	0.3	12.69	1.04	Al ⁺⁺	13.28	0.03
5	1.920397	0.3	3.63	0.91	Al ⁺⁺	12.47	0.09
6	1.920597	0.2	13.70	0.45	Al ⁺⁺	13.21	0.01
7	1.920898	1.1	5.57	2.18	Al ⁺⁺	12.42	0.19
8	1.921050	1.2	13.05	1.63	Al ⁺⁺	12.78	0.06
9	1.920804	1.3	3.62	1.70	Al ⁺⁺	12.19	0.19
10	1.921285	0.6	5.25	1.38	Al ⁺⁺	11.98	0.08
11	1.921431	0.4	6.28	0.53	Al ⁺⁺	12.30	0.02
1	1.920053	7.4	44.25	3.19	C ⁺³	14.47	0.11
2	1.920327	0.6	16.77	2.17	C ⁺³	16.80	0.68
3	1.920906	2.2	27.52	2.39	C ⁺³	14.12	0.05
4	1.921361	0.2	8.97	0.41	C ⁺³	13.96	0.02
5	1.921688	1.4	11.86	2.66	C ⁺³	13.09	0.17
6	1.921743	2.0	30.92	1.57	C ⁺³	13.82	0.05

Table 5b: FIT FOR $z=1.920$ – HIGH IONS

Comp	z	σ_z ($\times 10^{-5}$)	b (km s^{-1})	σ_b (km s^{-1})	Ion	$\log N$ (cm^{-2})	$\sigma_{\log N}$ (cm^{-2})
1	2.076214	0.1	5.75	0.23	Fe ⁺	13.34	0.02
					Al ⁺	12.19	0.01
1	2.076155	0.8	11.30	0.66	C ⁺³	13.45	0.03
2	2.076301	1.4	5.66	2.39	C ⁺³	12.84	0.32
3	2.076422	2.0	9.50	1.63	C ⁺³	13.22	0.10
4	2.076707	1.5	8.72	2.71	C ⁺³	12.21	0.09
1	2.076132	0.3	4.77	0.49	Si ⁺³	12.55	0.02
2	2.076393	0.6	11.03	1.00	Si ⁺³	12.54	0.03

Table 6: FIT FOR $z=2.076$ – LOW AND HIGH IONS

Comp	z	σ_z ($\times 10^{-5}$)	b (km s^{-1})	σ_b (km s^{-1})	Ion	$\log N$ (cm^{-2})	$\sigma_{\log N}$ (cm^{-2})
1	0.947779	0.1	2.23	0.17	Mg ⁺	12.64	0.04
					Fe ⁺	11.85	0.05
2	0.947861	0.5	4.15	1.72	Mg ⁺	11.47	0.07
3	0.948103	0.6	1.51	3.86	Mg ⁺	11.14	0.09
4	0.948336	0.1	3.12	0.27	Mg ⁺	13.09	0.06
					Fe ⁺	12.00	0.06
5	0.948389	0.4	6.11	0.42	Mg ⁺	12.69	0.04
					Fe ⁺	11.92	0.07

Table 7: FIT FOR $z=0.948$

Comp	z	σ_z ($\times 10^{-5}$)	b (km s^{-1})	σ_b (km s^{-1})	Ion	$\log N$ (cm^{-2})	$\sigma_{\log N}$ (cm^{-2})
1	1.016661	0.3	3.63	1.01	Fe ⁺	12.80	0.04
					Mg ⁰	10.82	0.07
2	1.016783	3.9	6.71	5.55	Fe ⁺	12.94	0.41
					Mg ⁰	10.78	0.46
3	1.016839	0.7	3.04	1.80	Fe ⁺	13.08	0.26
					Mg ⁰	11.04	0.24
4	1.016935	0.3	4.59	1.24	Fe ⁺	12.91	0.05
					Mg ⁰	11.04	0.06
5	1.017026	0.6	4.02	2.21	Fe ⁺	12.48	0.11
					Mg ⁰	10.83	0.10
6	1.017156	0.1	6.10	0.26	Fe ⁺	14.00	0.01
					Mg ⁰	11.93	0.01
7	1.017256	0.2	5.63	0.29	Fe ⁺	13.74	0.02
					Mg ⁰	11.70	0.02

Table 8: FIT FOR $z=1.107$

Comp	z	σ_z ($\times 10^{-5}$)	b (km s^{-1})	σ_b (km s^{-1})	Ion	$\log N$ (cm^{-2})	$\sigma_{\log N}$ (cm^{-2})
1	2.013144	0.9	19.21	1.24	C ³⁺	12.95	0.02
2	2.014375	0.1	7.99	0.25	C ³⁺	13.71	0.01
			5.23	0.25	Si ³⁺	12.95	0.02
3	2.014408	2.3	38.72	3.30	C ³⁺	13.32	0.04
			25.32	3.30	Si ³⁺	12.38	0.06
4	2.014544	0.7	5.90	1.01	C ³⁺	12.80	0.06
5	2.014900	2.6	13.64	3.95	C ³⁺	12.40	0.17

Table 9: FIT FOR $z=2.014$

Transition	Apparent	VPFIT	EqW	Adopted
FeII 1611	15.461 ± 0.020	15.454 ± 0.058		15.458 ± 0.058
NiII 1709	13.902 ± 0.010	13.880 ± 0.054		
NiII 1741	13.878 ± 0.006			
NiII 1751	13.912 ± 0.010			
SiII 1808	15.794 ± 0.005	15.807 ± 0.059		15.801 ± 0.059
CrII 2056	13.628 ± 0.009	13.645 ± 0.062		13.753 ± 0.062
CrII 2066	13.681 ± 0.013			
ZnII 2026	12.935 ± 0.009	12.912 ± 0.057		12.924 ± 0.057
CuII 1358	12.992 ± 0.063		12.929 ± 0.068	12.962 ± 0.065
GeII 1602	< 12.430		< 12.431	< 12.430
TiII 1910			12.807 ± 0.038	12.807 ± 0.038
C IV 1548		16.804 ± 0.675		16.804 ± 0.675
AlIII 1854	13.874 ± 0.003	13.887 ± 0.013		13.881 ± 0.013

Table 10: IONIC COLUMN DENSITIES FOR $z = 1.920$

Note. — Values reported in logarithmic space have deceptively small errors. For instance, the value for $N(\text{Cu})$ is not a 5σ detection.

Transition	Apparent	VPFIT	EqW	Adopted
FeII 1608	13.296 ± 0.018	13.342 ± 0.016		13.320 ± 0.016
AlII 1670	12.174 ± 0.012	12.194 ± 0.014		12.184 ± 0.014
SiII 1304	13.756 ± 0.037			13.756 ± 0.037
C II 1334	14.151 ± 0.069			> 14.151
NiII 1751	< 12.289		< 12.305	< 12.297
CrII 2056	12.12 ± 0.12		12.10 ± 0.13	12.11 ± 0.13
ZnII 2026	< 11.330		< 11.342	< 11.336
Si IV 1402	12.833 ± 0.019	12.848 ± 0.017		
C IV 1548	13.713 ± 0.005	13.727 ± 0.055		

Table 11: IONIC COLUMN DENSITIES FOR $z = 2.076$

Transition	Apparent	Adopted
FeII 2374	14.611 ± 0.030	14.611 ± 0.030
FeII 2260	14.743 ± 0.084	
MgI 2852	12.364 ± 0.006	12.364 ± 0.006
MnII 2606	12.420 ± 0.053	12.532 ± 0.053
MnII 2594	12.386 ± 0.051	
MnII 2576	12.641 ± 0.018	
TiII 3073	12.243 ± 0.067	12.300 ± 0.030
TiII 3242	12.319 ± 0.034	
TiII 3384	12.228 ± 0.021	

Table 12: IONIC COLUMN DENSITIES FOR $z = 0.752$

Transition	Apparent	VPFIT	Adopted
FeII 2382	12.318 ± 0.050	12.401 ± 0.034	12.401 ± 0.034
FeII 2586	11.936 ± 0.391		
FeII 2600	12.452 ± 0.046		
MgII 2796	13.069 ± 0.008	13.342 ± 0.038	13.342 ± 0.038
MgII 2803	13.146 ± 0.006		
MgI 2852	10.81 ± 0.15		10.81 ± 0.15

Table 13: IONIC COLUMN DENSITIES FOR $z = 0.948$

Transition	Apparent	VPFIT	Adopted
FeII 2344	14.168 ± 0.086		
FeII 2374	14.242 ± 0.008	14.285 ± 0.026	14.285 ± 0.026
FeII 2586	14.212 ± 0.007	14.285 ± 0.026	
MgI 2852	12.236 ± 0.007	12.247 ± 0.024	12.247 ± 0.024

Table 14: IONIC COLUMN DENSITIES FOR $z = 1.017$

Metal	$\log_{10}N(X)$ (cm^{-2})	[X/H]
Fe	15.458 ± 0.058	-0.705 ± 0.097
Ni	13.891 ± 0.054	-1.012 ± 0.095
Si	15.801 ± 0.059	-0.402 ± 0.098
Cr	13.753 ± 0.062	-0.580 ± 0.100
Ti	12.807 ± 0.038	-0.776 ± 0.081
Zn	12.924 ± 0.057	-0.379 ± 0.097
Cu	12.962 ± 0.065	0.039 ± 0.102
Ge	< 12.430	< 0.147

Table 15: ABUNDANCES FOR $z = 1.920$

Metal	$\log_{10}N(X)$ (cm^{-2})	[X/H]
Fe	13.320 ± 0.016	-2.621 ± 0.071
Al	12.184 ± 0.014	-2.727 ± 0.070
Si	13.756 ± 0.037	-2.225 ± 0.075
Ni	< 12.297	< -2.384
Cr	12.11 ± 0.13	-2.00 ± 0.15
Zn	< 11.336	< -1.745
C	> 14.151	> -2.840

Table 16: ABUNDANCES FOR $z = 2.076$

REFERENCES

- Anders, M.V., & Grevesse, N. 1989, *Geochim. Cosmochim. Acta*, 53, 197
- Barlow, T. 1996, in preparation.
- Bergeron, J. and Petitjean, P. 1991, *A & A*, 241, 365
- Cardelli, J.A. 1994, *Science*, 265, 209.
- Cox, D. P. 1970, Ph. D. thesis, University of California at San Diego
- Evardsson, B., Anderson, J., Gutasfsson, B., Lambert, D.L., Nissen, P.E., and Tompkin, J. 1993, *Astronomy and Astrophysics*, 275, 101.
- Lu, L., Savage, B. D., Tripp, T. M., and Meyer, D. M. 1995, *ApJ*, 447, 597
- Lu, L., Sargent, W., & Barlow, T.A. 1995, to appear in *Cosmic Abundances: The Proceedings of the 6th Annual October Astrophysical Conference in Maryland*
- Lu, L., in preparation
- Lu, L., in preparation
- Madau, P. 1992, *ApJ*, 335, 498
- Pettini, M., Smith, L. J., Hunstead, R. W., and King, D. L. 1994, *ApJ*, 426, 79
- Prochaska, J.X. and Wolfe, A.M., 1996, *ApJ*, 470, in press
- Prochaska, J.X. and Wolfe, A.M., in preparation
- Rauch, M., Carswell, R.F., Robertson, J.G., Shaver, P.A., and Webb, J.K. 1990, *MNRAS*, 242, 698
- Rauch, M., Carswell, R.F., Webb, J.K., and Weymann, R.J. 1993, *MNRAS*, 260, 589
- Robertson, J.G., Shaver, P.A., Carswell, R.F. 1983, in *Quasars and Gravitational Lenses*, ed. J.P. Swings (Liège: Université de Liège), p. 602
- Savage, B. D. and Sembach, K. R. 1991, *ApJ*, 379, 245
- Sembach, K.R., Steidel, C.C., Macke, R.J., and Meyer, D.M. 1995, *ApJ*, 445, L27
- Shull, J.M. and Van Steenberg, M. 1982, *ApJS*, 48, 95

- Sneden, C., Gratton, R.G., & Crocker, D.A. 1991, *A & A*, 246, 354
- Spitzer, L. and Fitzpatrick, E.L. 1993, *ApJ*, 409, 299
- Spitzer, L., & Fitzpatrick, E.L. 1993, *ApJ*, 445, 196
- Storrie-Lombardi, L. J., McMahon, R. G., Irwin, M.J., & Hazard, C. 1995, in *ESO Workshop on QSO Absorption Lines*, ed. G. Meylan, (Berlin:Springer-Verlag).
- Vogt, S. S. 1992, in *ESO Conf. and Workshop Proc. 40, High Resolution Spectroscopy with the VLT*, ed. M.-H. Ulrich (Garching: ESO), p. 223
- Wheeler, J.C., Sneden, C., & Truran, J.W.Jr. 1989, *ARA & A*, 27, 279
- Wolfe, A. M., Fan, X-M., Tytler, D., Vogt, S. S., Keane, M. J., & and Lanzetta, K. M. 1994, *ApJ*, 435, L101
- Wolfe, A. M. 1995, in *ESO Workshop on QSO Absorption Lines*, ed. G. Meylan, (Berlin:Springer-Verlag)
- Wolfe, A. M., et al. 1996, in preparation
- York, D. G., Green, R. F., Bechtold, J., and Chafee, F. H. 1984, *ApJ*, 280, L1

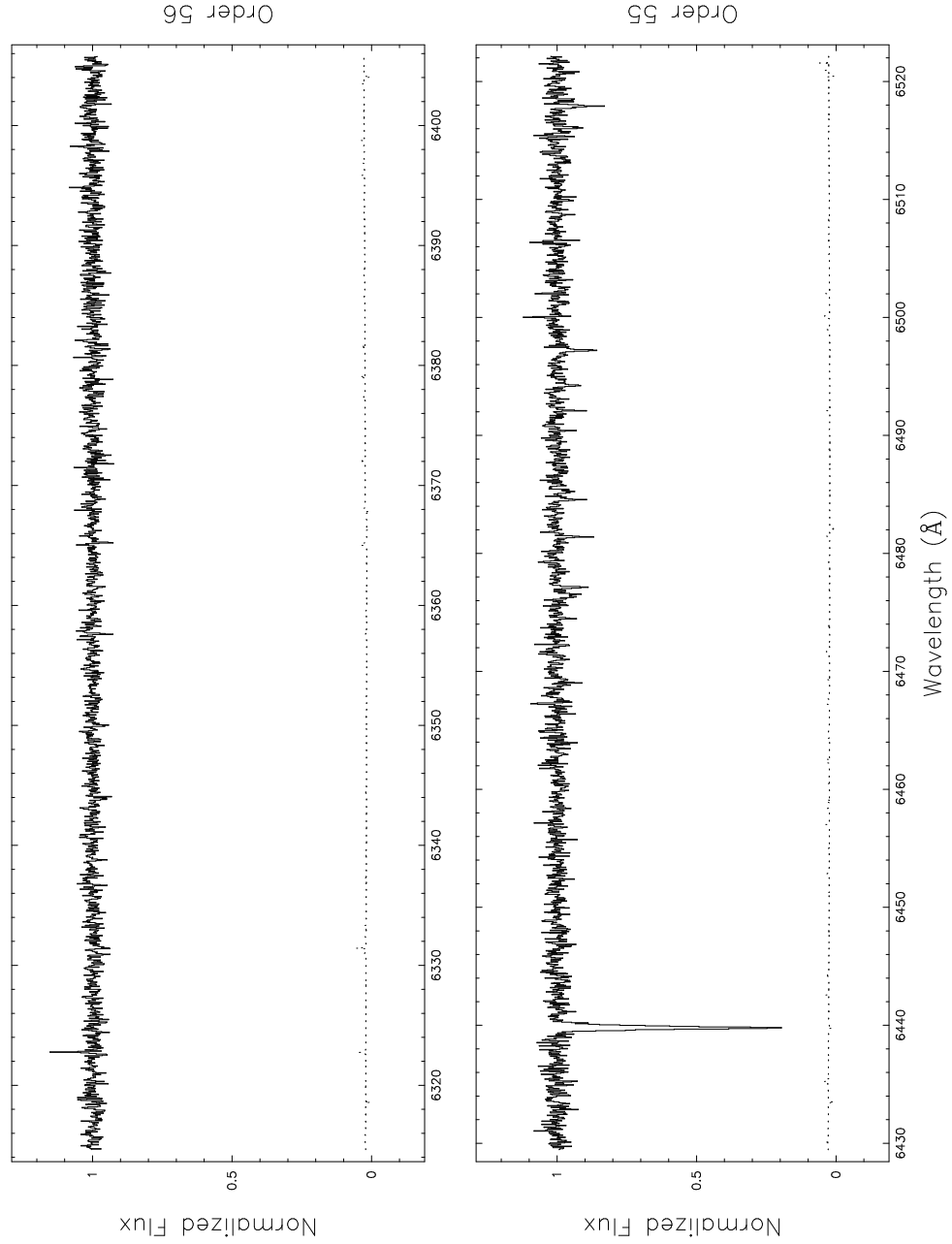


Fig. 1.— Keck HIRES spectra of Q2206-199 at a resolution of $\approx 8 \text{ km s}^{-1}$ and a SNR of ≈ 45 . All 36 orders presented are identified by the echelle order intrinsic to the Keck HIRES spectrograph. The dotted line is a 1σ error array derived assuming Poisson statistics.

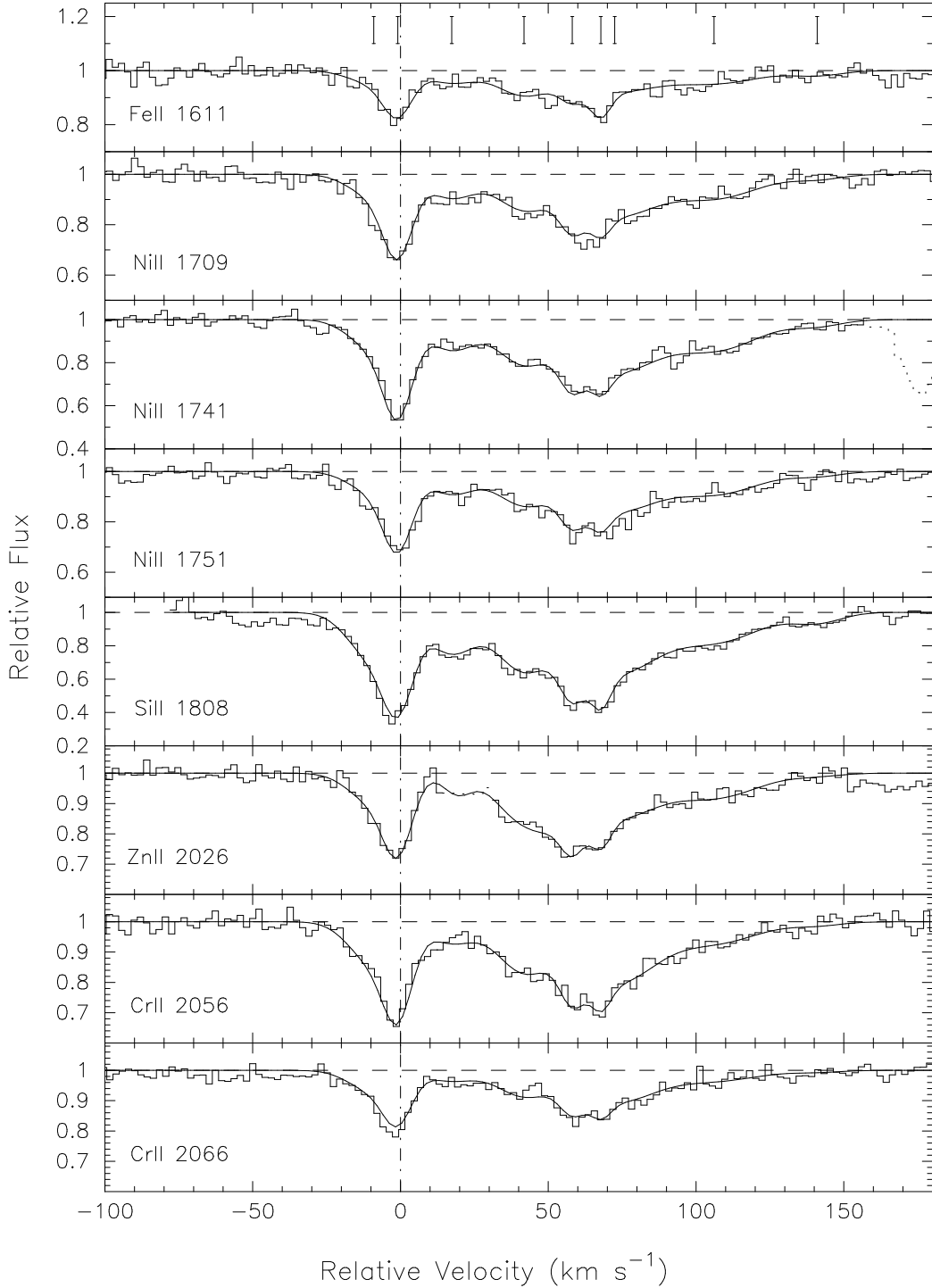


Fig. 2.— Velocity profiles of the low-ion transitions from the system at $z=1.920$. The overplotted curve represents the least-squares VPFIT solution to the 8 transitions. The dotted profile indicates blends from intervening systems. The dashed vertical line corresponds to $z=1.920$. The marks above the Fe II 1611 indicate the velocity centroids for the VPFIT solution as listed in Table 5a. In all figures with VPFIT solutions, the leftmost mark is component 1.

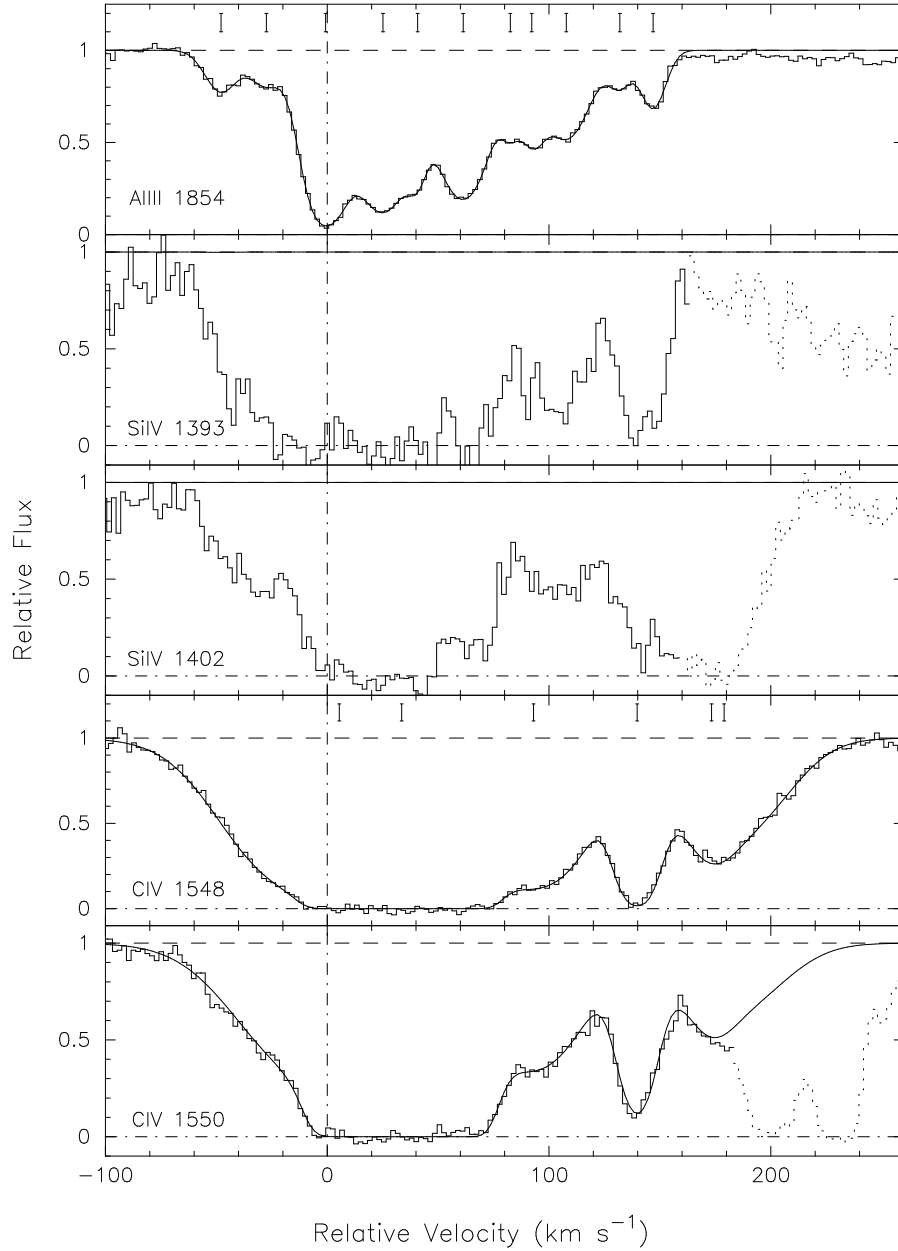


Fig. 3.— Velocity profiles and VPFIT solutions of the high-ion and Al III transitions from the system at $z=1.920$. The dashed vertical line corresponds to $z=1.920$. The dotted profile indicates blends from intervening systems.

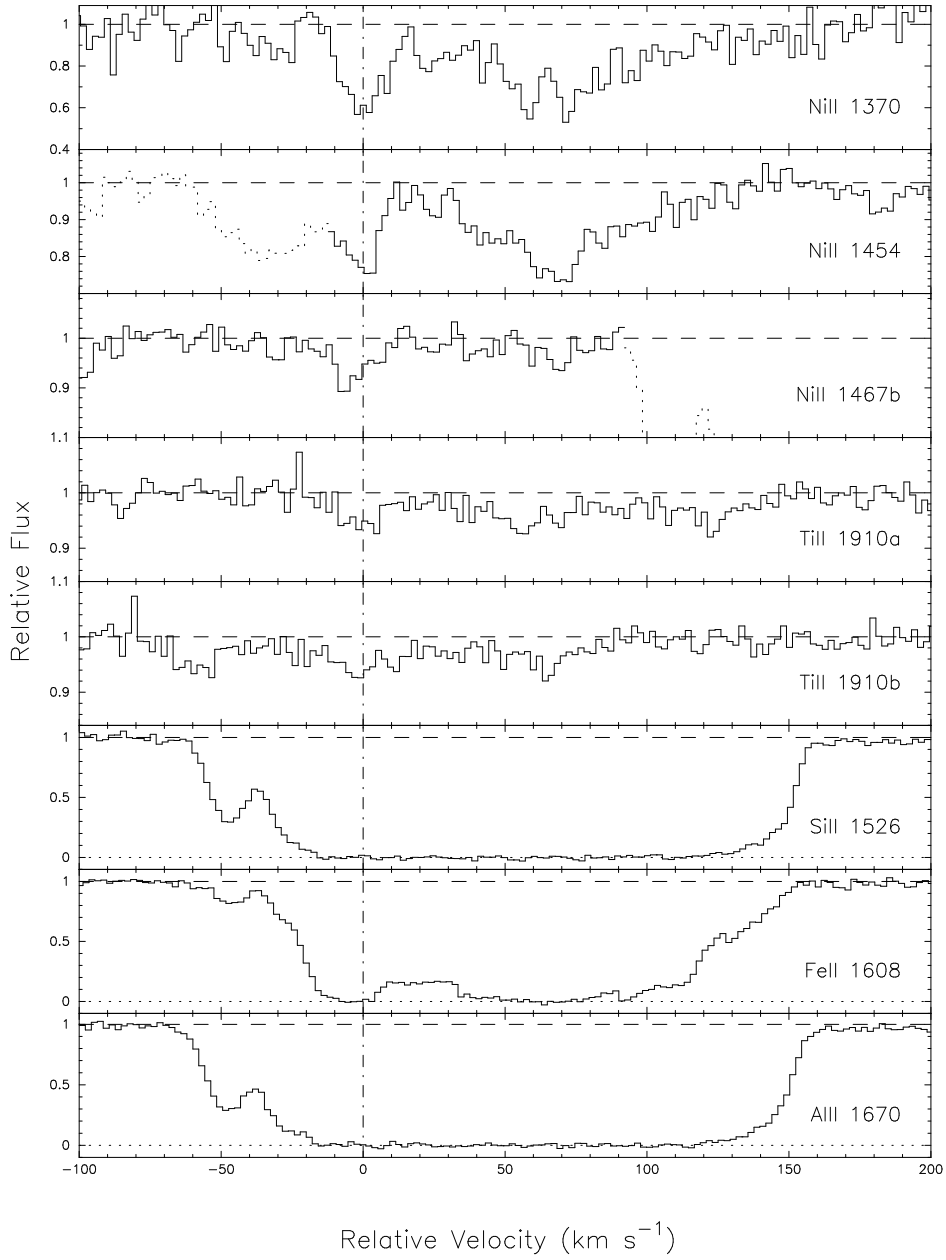


Fig. 4.— Velocity profiles of those metal-line transitions from the system at $z = 1.920$ without VPFIT solutions. The dashed vertical line is at $z=1.920$.

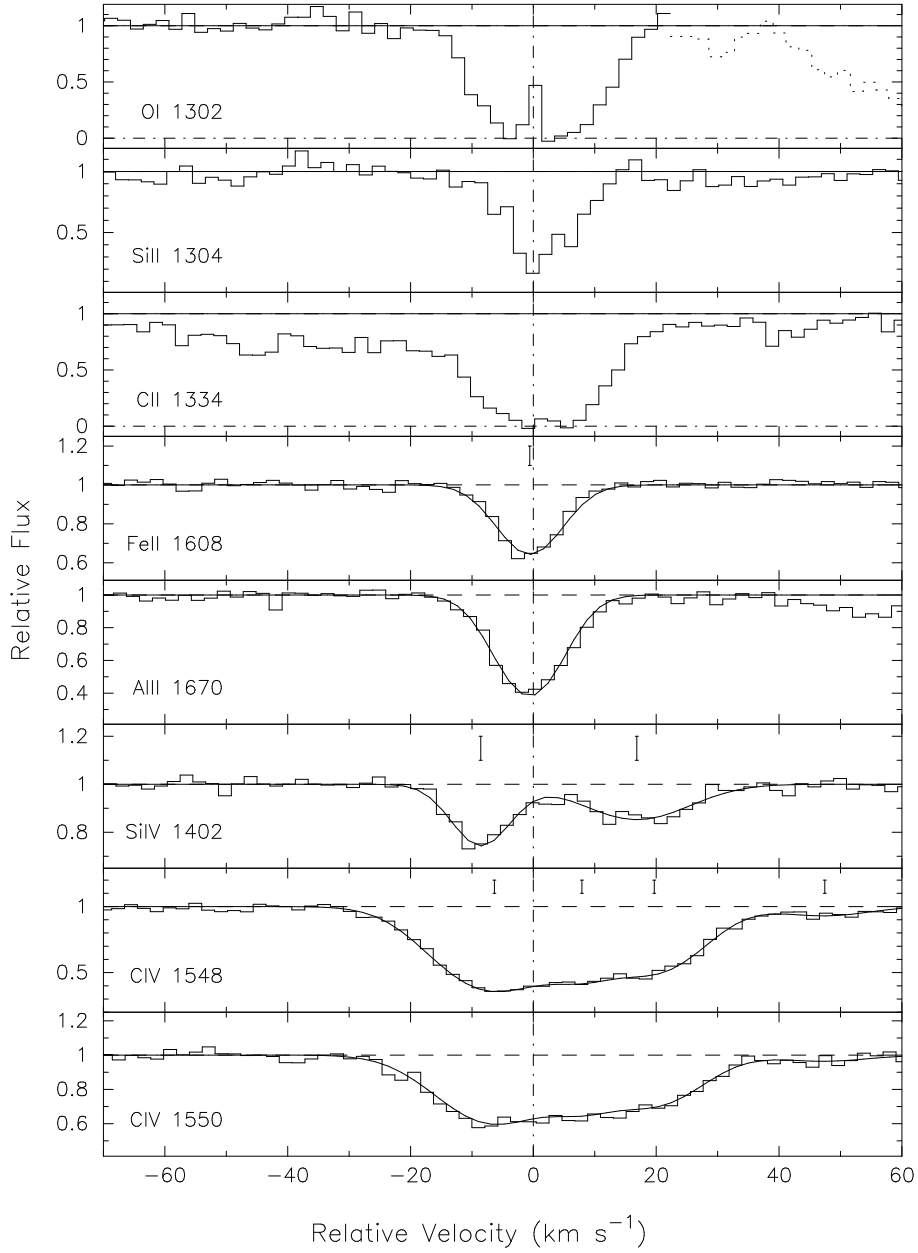


Fig. 5.— Velocity profiles and VPFIT solutions for the transitions from the system $z=2.076$. The dashed vertical line corresponds to $z=2.07623$.

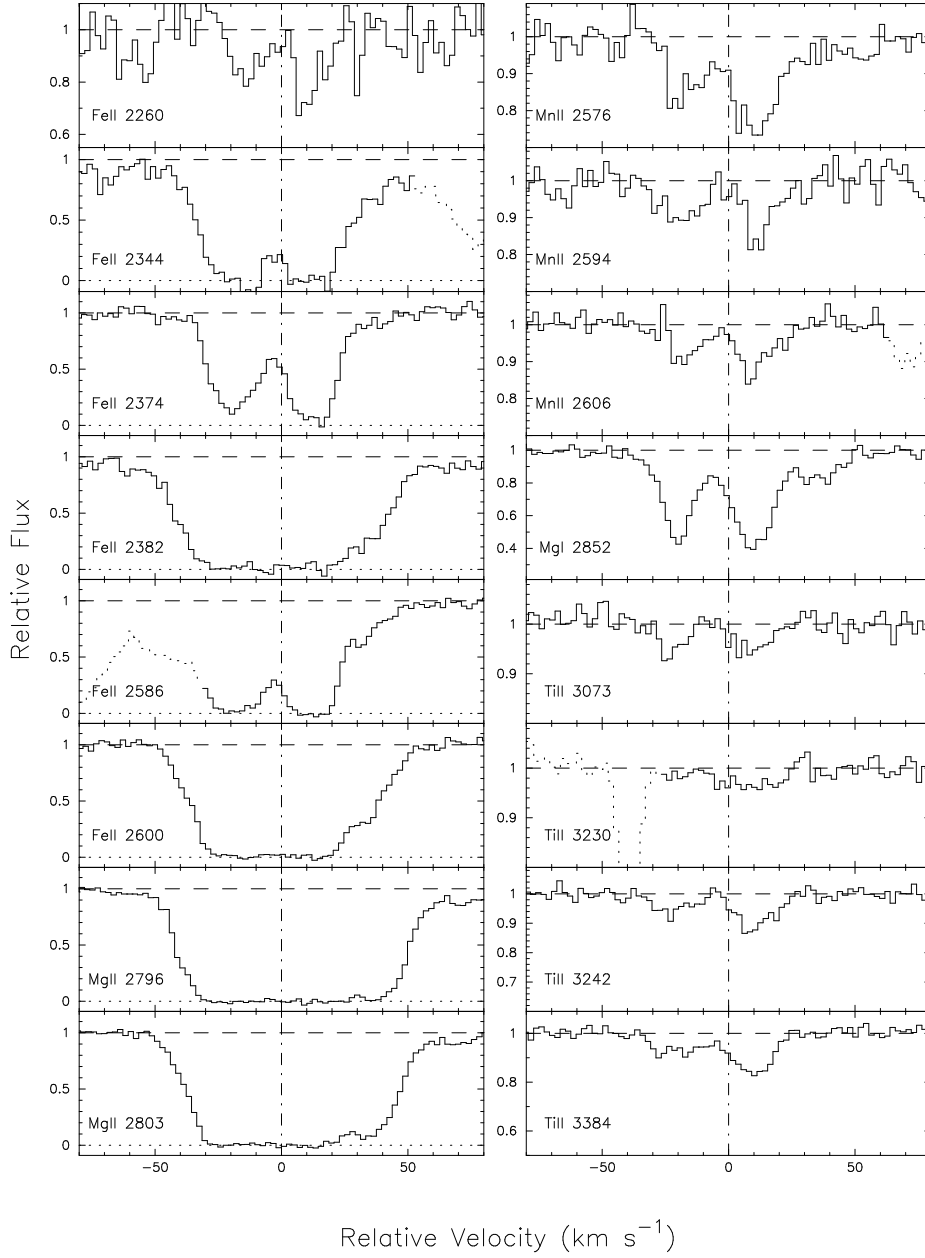


Fig. 6.— Velocity profiles of the Mg II metal system at $z=0.752$. The dashed vertical line is at $z=0.7519$.

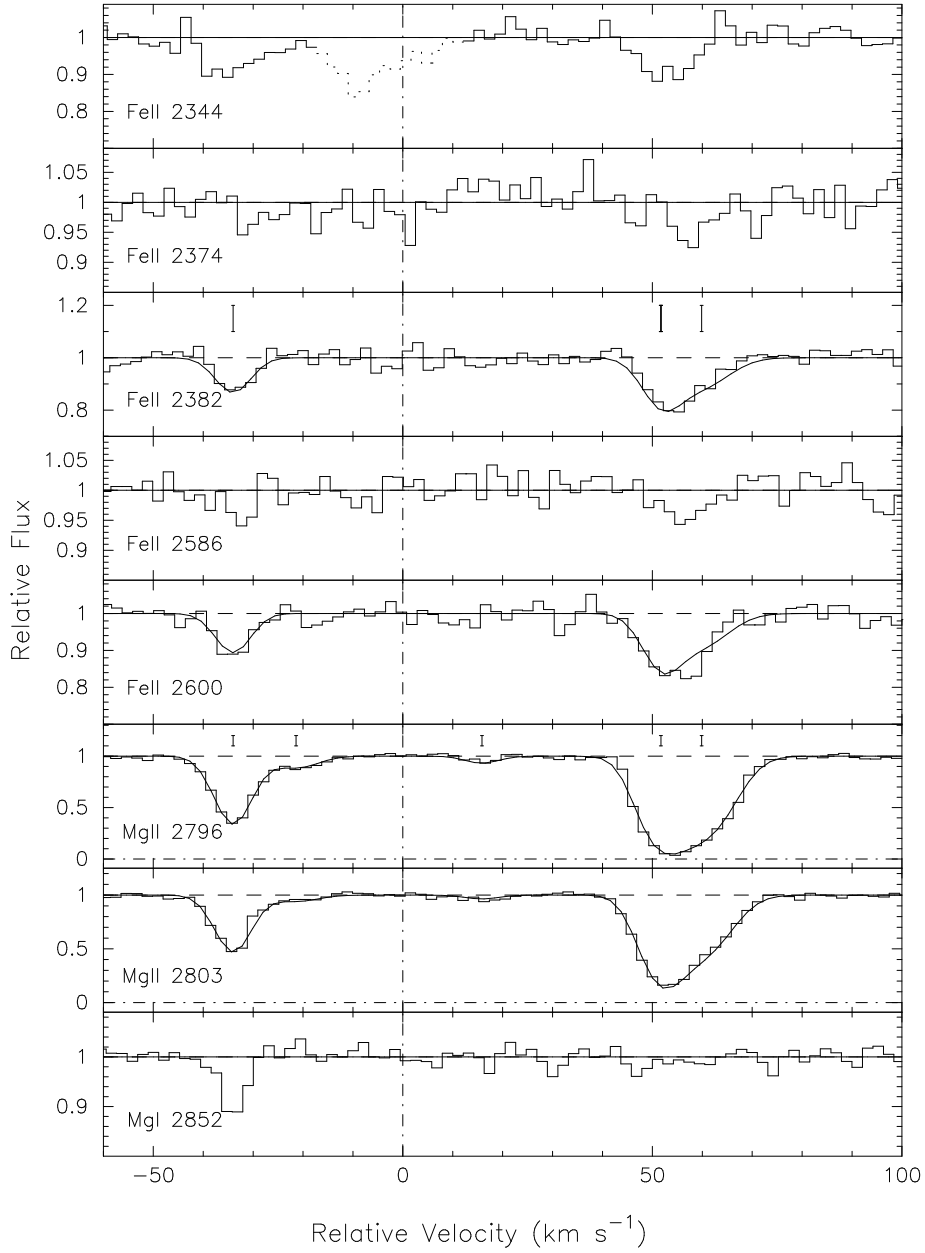


Fig. 7.— Velocity profiles and VPFIT solutions of the Mg II metal system at $z=0.948$. The dashed vertical line corresponds to $z=0.948$

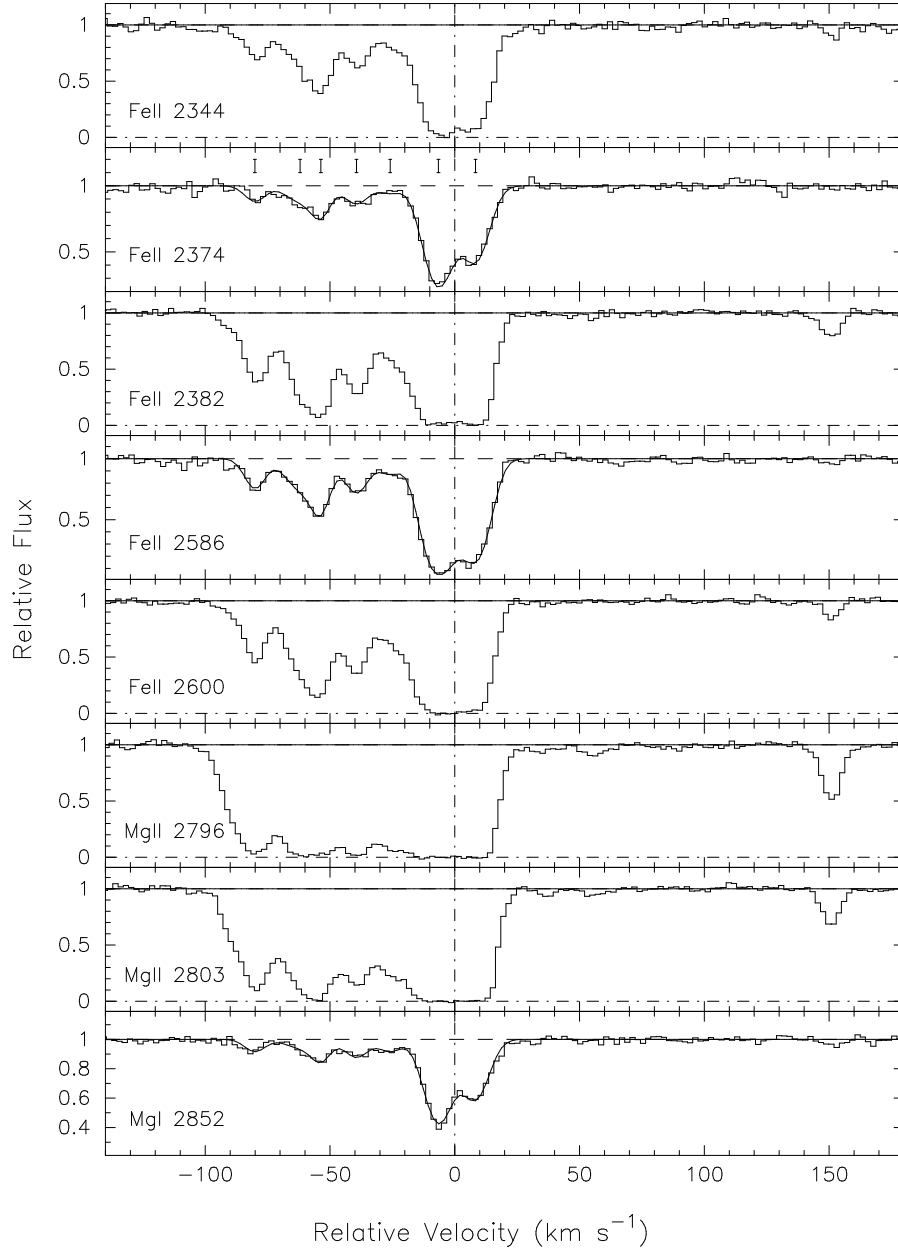


Fig. 8.— Velocity profiles and VPFIT solutions of the Mg II metal system at $z=1.017$. The dashed vertical line is at $z=1.10172$.

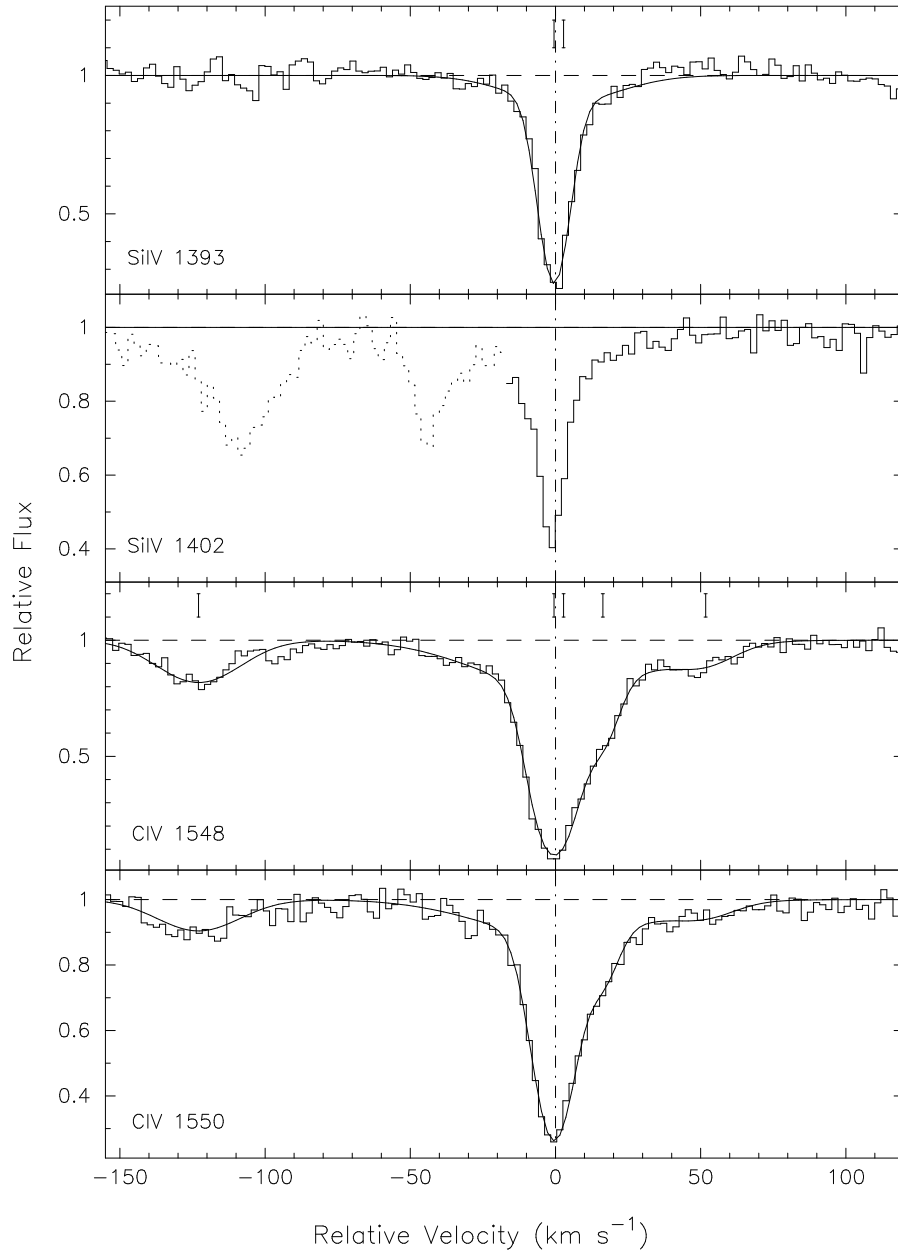


Fig. 9.— Velocity profiles and VPFIT solutions of the C IV system at $z=2.014$. The high-ion profiles are very narrow, indicating the system was not collisionally ionized. The dashed vertical line corresponds to $z=2.01438$.

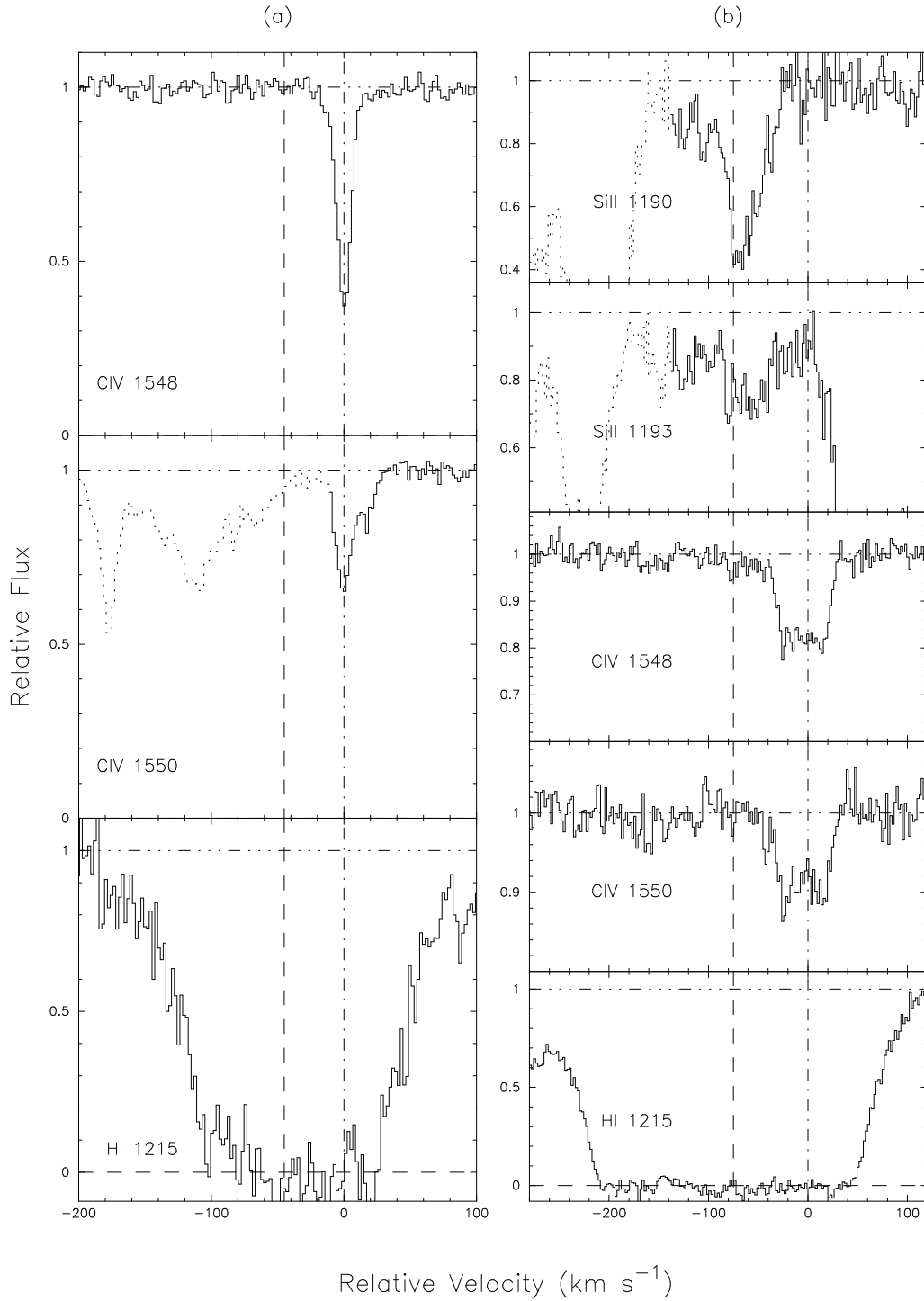


Fig. 10.— Velocity profiles of the C IV systems at (a) $z=2.281$ and (b) $z = 2.445$. Note in each case the displacement of the center of the C IV doublet from the center of the Ly α profile. This is direct evidence that high-ions do not trace HI gas.

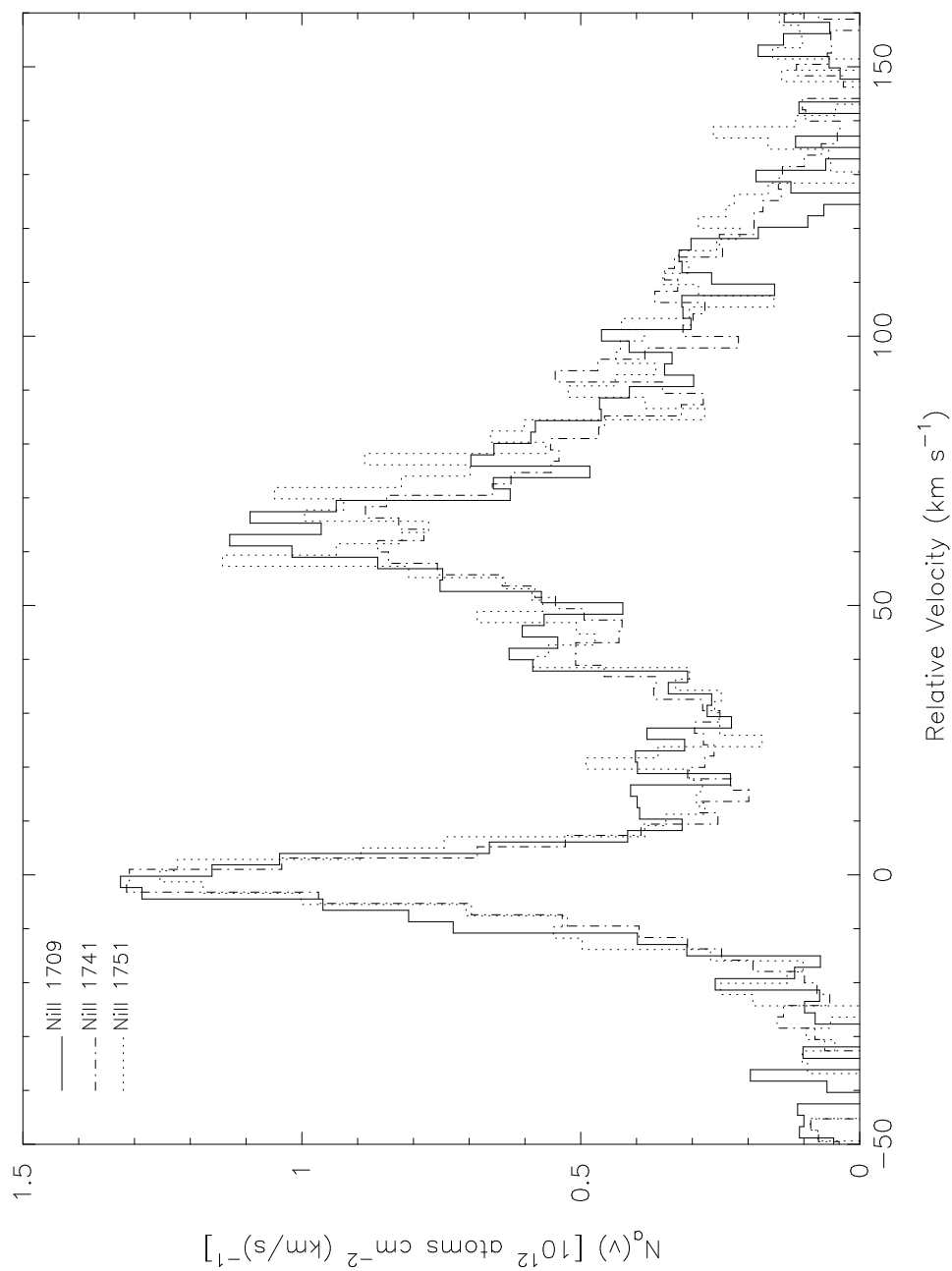


Fig. 11.— Apparent column density $[N_a(v)]$ profiles for Ni II 1709, 1741, and 1751 in the $z=1.920$ system. Note that where the profile of the weakest transition (Ni II 1709) dominates, this is evidence for hidden saturation. Therefore, the divergence of the profiles near the features at $v \approx 65 \text{ km s}^{-1}$ indicates hidden line saturation.

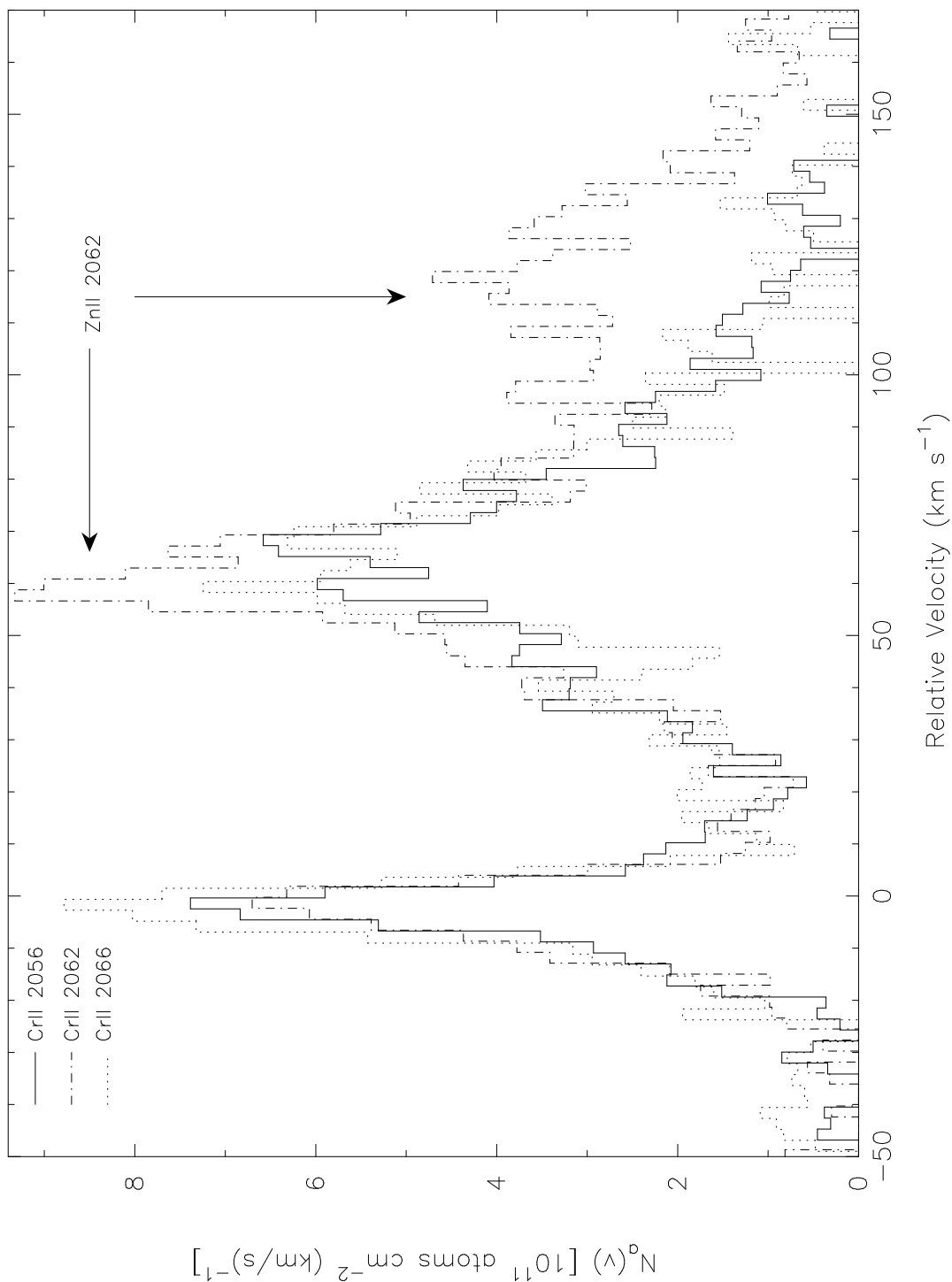


Fig. 12.— Apparent column density $[N_a(v)]$ profiles for Cr II 2056, 2062, and 2066 in the $z=1.920$ system. Note that where the profile of the weakest transition (Cr II 2066) dominates, this is evidence for hidden saturation. Therefore, the divergence of the profiles at $v = 3 \text{ km s}^{-1}$ indicates hidden saturation. The overabundance of Cr II 2062 at $v > 40 \text{ km s}^{-1}$ is due to line blending with Zn II 2062.

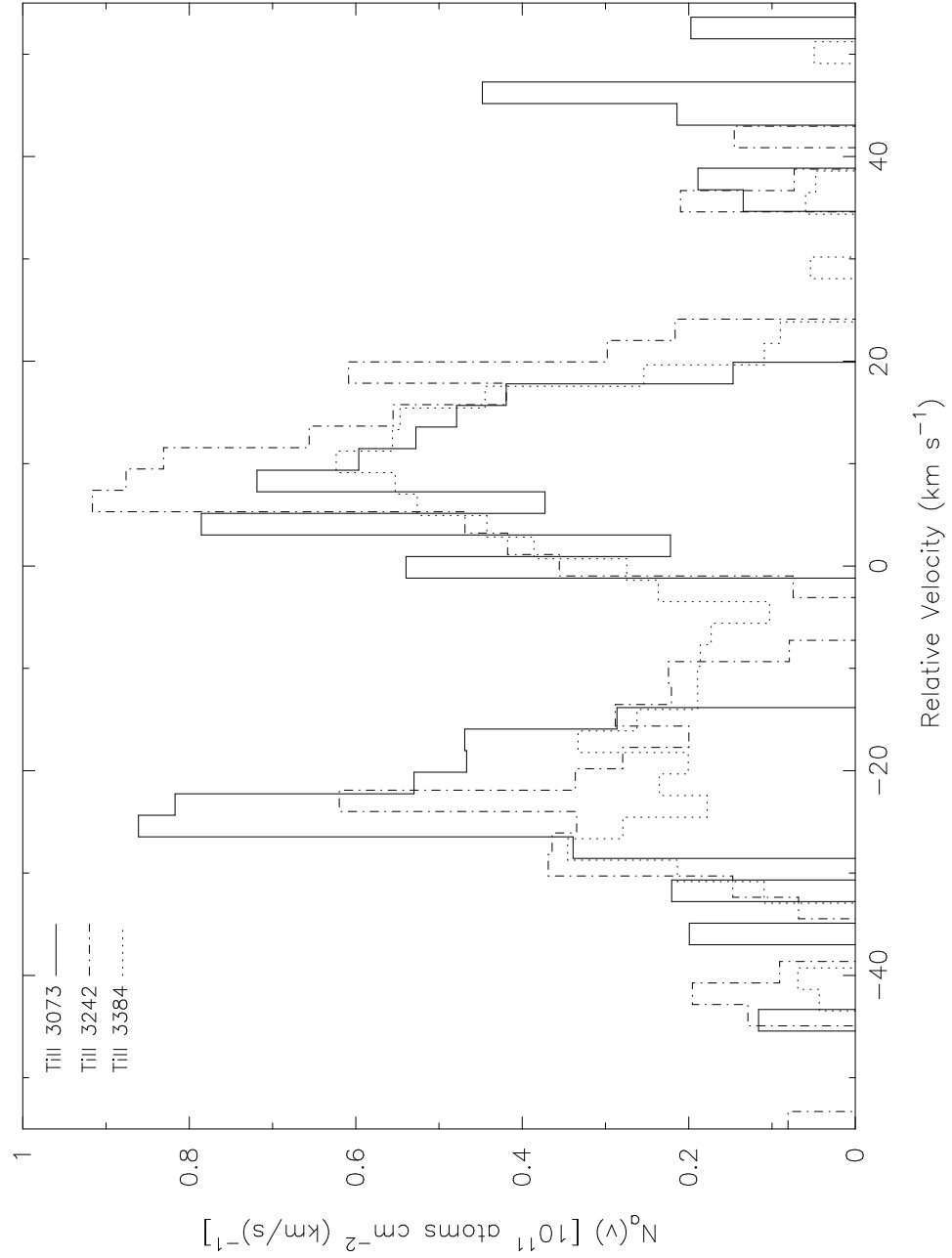


Fig. 13.— Apparent column density $[N_a(v)]$ profiles for Ti II 3073 3242, and 3384 in the $z=0.752$ system. The divergence of the profiles at $v = -20 \text{ km s}^{-1}$ may indicate hidden saturation.

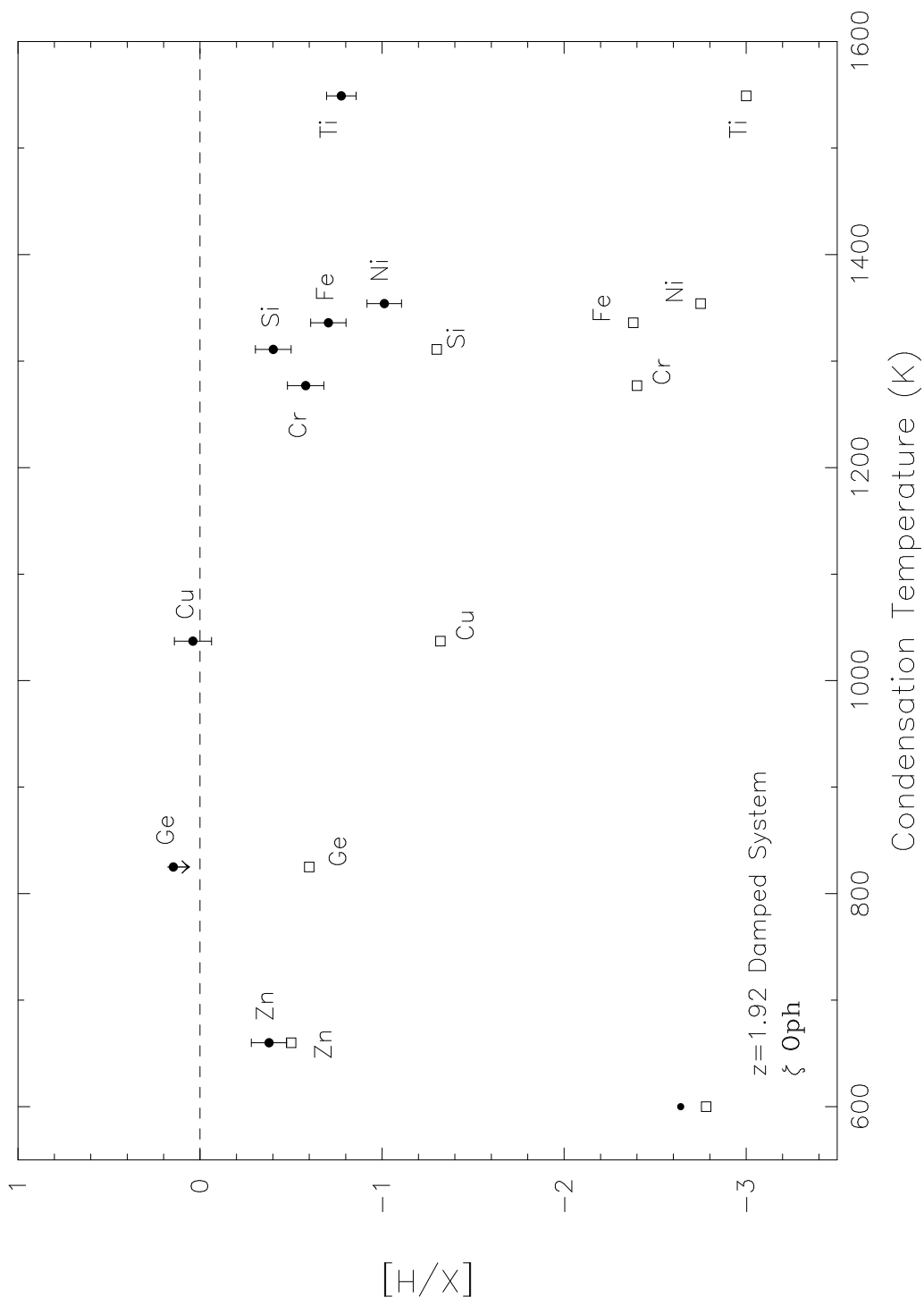


Fig. 14.— Logarithmic abundances of the low-ions Fe, Cr, Si, Ni, Zn, Cu and Ge relative to standard solar abundances versus condensation temperatures for the $z=1.920$ system (solid dots) and for the line of sight in the ISM toward ζ Oph (open squares). Error in the neutral Hydrogen column density dominates the error associated with these measurements such that the error in relative abundances of the metals is significantly smaller.

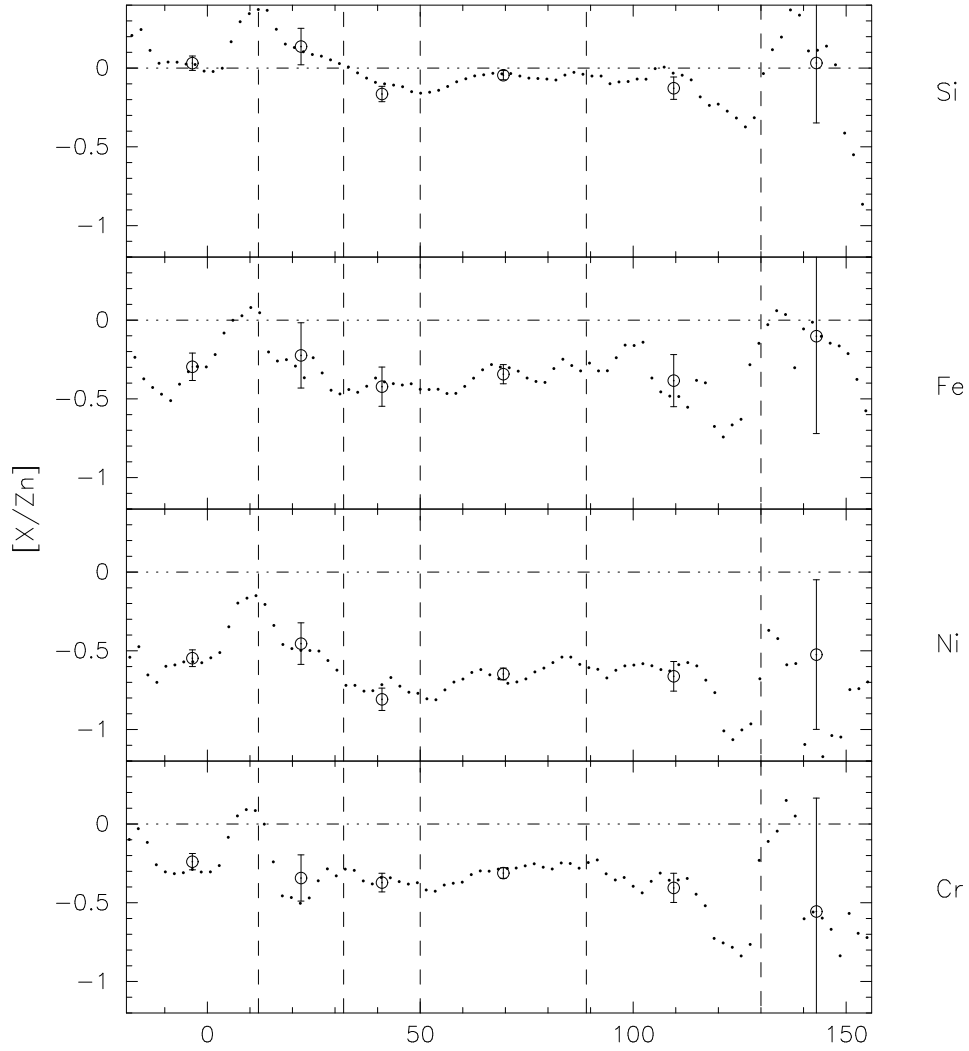


Fig. 15.— Relative cosmic abundances of Fe, Ni, Si, and Cr versus Zn for the $z = 1.920$ system. The small points mark the relative abundance average over 5 pixels at the given velocity. The large points denote the relative abundance over the velocity intervals marked by the large tick marks. The dot-dash line at 0 represents zero depletion with respect to Zn.

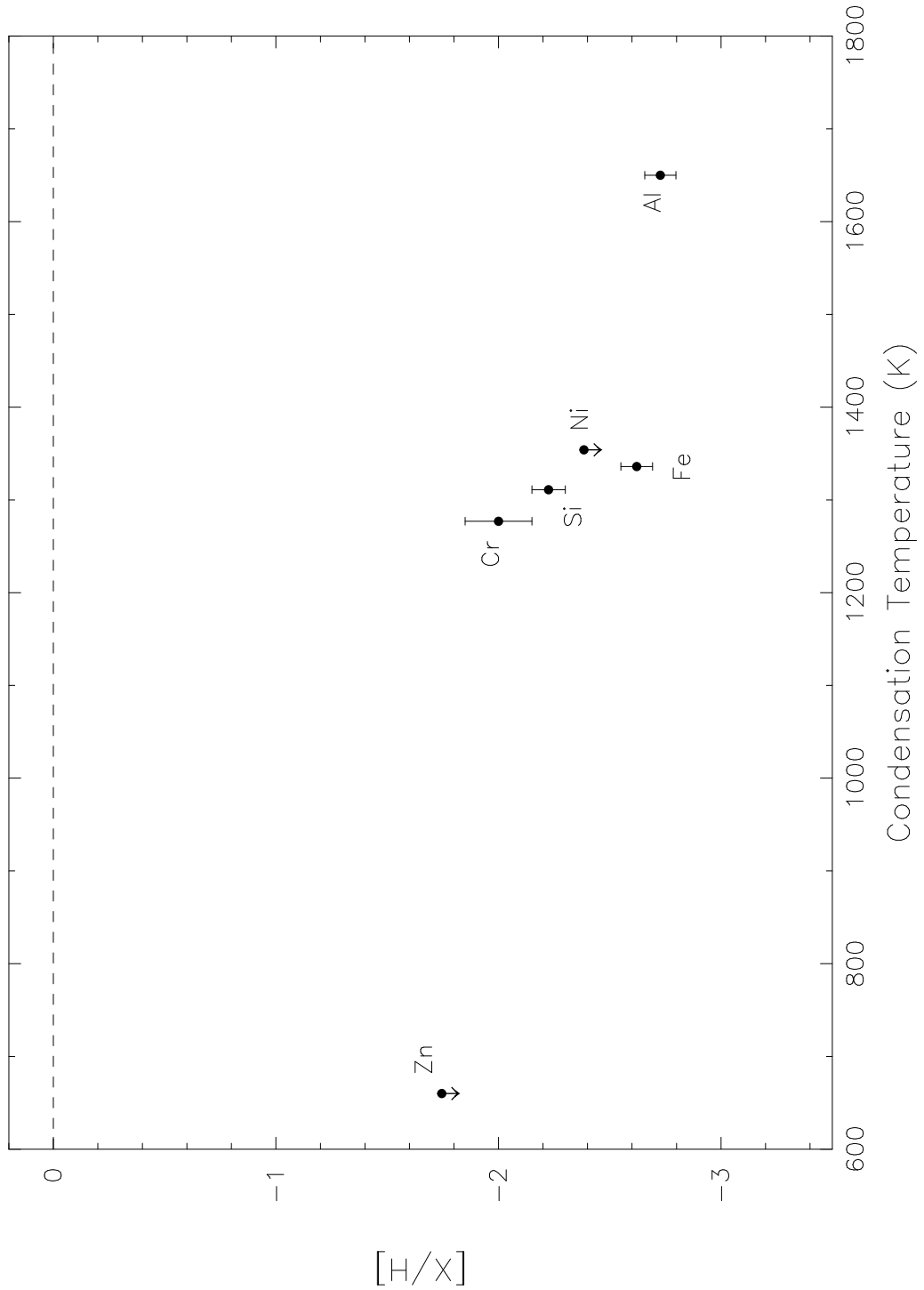


Fig. 16.— Abundances of the low-ions Fe, Cr, Si, Ni, Zn, and Al versus their condensation temperatures for the $z=2.076$ system. Note that with the exception of Cr, the error in the neutral Hydrogen column density dominates the error associated with these measurements.